universität wien

MASTERARBEIT | MASTER'S THESIS

Titel | Title

Production of Composite Materials with a Nanostructured Interface

verfasst von | submitted by

Florian Gregor BSc

angestrebter akademischer Grad | in partial fulfilment of the requirements for the degree of

Diplom-Ingenieur (Dipl.-Ing.)

Wien | Vienna, 2025

Studienkennzahl lt. Studienblatt | Degree programme code as it appears on the student record sheet:	UA 066 658
Studienrichtung lt. Studienblatt | Degree programme as it appears on the student record sheet:	Masterstudium Chemie und Technologie der Materialien
Betreut von | Supervisor:	Univ.-Prof. Dr. Alexander Bismarck

Abstract

To enable production of strong but tough carbon fibre reinforced composite materials, a brick-and-mortar type interface layer, was to be deposited on carbon fibres by means of electrophoretic deposition. This layer, a functional analogue to natural Nacre, shall lead to increased toughness through properties like crack deflection and strain hardening. To facilitate this, a stable aqueous suspension of layered double hydroxide particles was successfully produced at bench scale and decalitre scale. Electrophoretic deposition was carried out at both scales, resulting in continuous production of hierarchical composite laminates with a nanostructured layered double hydroxide interface. Within the examined fibre/matrix system, interlaminar shear strength was not found to be dependent upon deposition of a brick-and-mortar type interface.

Abstract

Um die Produktion von Carbonfaser-Verbundwerkstoffen zu ermöglichen, welche hohe Zugfestigkeit mit hoher Widerstandskraft kombinieren, sollte eine nanostrukturierte Schicht aus biomimetischen, perlmuttartigen Plättchen mittels elektrophoretischer Deposition an der Faser/Matrix Grenzfläche abgeschieden werden. Eine solche Schicht ermöglicht weniger abruptes Materialversagen durch den Einsatz von Mechanismen zur Dehnungsverfestigung und Ablenkung von Rissen entlang der Oberfläche der Plättchen. Dazu wurde eine stabile, wässrige Suspension aus Schichtdoppelhydroxiden im kleinen und großen Labormaßstab hergestellt. Elektrophoretische Deposition konnte damit in beiden Maßstäben durchgeführt werden. Dadurch konnte die kontinuierliche Produktion von Komposit-Laminaten mit nanostrukturierter Grenzfläche realisiert werden. Negative Einflüsse durch diese Grenzfläche auf die interlaminare Scherfestigkeit im gegebenen Faser/Matrix System konnten nicht nachgewiesen werden.

Acknowledgements

I want to thank Prof. Alexander Bismarck for giving me the opportunity to get a glimpse of academic life by letting me pursue the final steps of my master's education at PaCE group. I also want to thank Diana Bratilescu for dedicating time during her workdays to patiently explain concepts and practical aspects of lab work to me, for the many bits and pieces of useful feedback I received and for always having time for me, despite her many other obligations. Furthermore, I want to thank Alex and Diana both for giving me the freedom to pursue research objectives independently. Further thanks go out to all the other members of PaCE who welcomed me into their group and shared lab benches, time during break and afterwork beers with me.

Abbreviations

CF ... carbon fibre

DLS ... dynamic light scattering

EPD ... electrophoretic deposition

FDM ... fused deposition modelling

FRP ... fibre reinforced plastic

FTIR ... Fourier-transformed infrared spectroscopy

FWF ... fibre weight fraction

ILSS ... interlaminar shear strength

IR ... infrared

LDH ... layered double hydroxide

LDO ... layered double oxide

PDDA ... poly(diallyldimethylammonium)chloride

PEI ... polyetherimide

PMMA ... polymethylmethacrylate

PSS ... polystyrene sulfonate

SEM ... scanning electron microscopy

TGA ... thermogravimetric analysis

XPS ... x-ray photoelectron spectroscopy

XRD ... x-ray diffractometry

Table of contents

Abstract 2
Abstract 3
Acknowledgements 4
Abbreviations 5
1. Introduction 7
1.1. Composite Materials 7
1.2. Nacre: structure and mechanical properties 8
1.3. Nacre micromimetics in FRPs 9
1.4. The LDH/PSS system and its deposition onto carbon fibres 10
1.5. Electrophoretic deposition for continuous coating of fibres 11
1.6. Motivation and aim 12
2. Materials and methods 13
2.1. Materials 13
2.2. Methods 13
3. Results 21
3.1. LDH platelets 21
3.2. LDH suspension 25
3.3. LDH-coating of carbon fibres 26
3.4. Production of CF/LDH/PEI composites 31
4. Conclusion 34
5. Outlook 35
5.1. Deposition of an LDH/polymer assembly 35
5.2. Electrocoagulation 35
6. Appendix 36
6.1. Measurements 36
6.2. Table of figures 61
6.3. Bibliography 64

1. Introduction

1.1. Composite Materials

Conjoining two or more constituent materials with different mechanical properties by means of an interface will result in a composite material.[1] The basic concept of combining materials with different properties that complement one another is nothing new – a famous piece of old technology being the composite bow constructed from horn and tendon used by nomadic equestrian cultures of the central Asiatic steppes in the late antique age.[2] Further examples include ceramics reinforced by natural fibres as early as 6500 BC[3] or clay bricks reinforced by straw used by the ancient Egyptians.[4]

Engineered composite materials began to be developed in the modern industrial age, when the demand for better performing warplanes prompted initial research into FRPs (fibre reinforced plastics) in the 1930s.[5] High-performance reinforcements such as polyacrylonitrile based carbon fibres started to be developed in the 1960s.[6] Coupled with the availability of more advanced resin systems as well as alternative matrices such as ceramics or metals, composite systems can be tailored to any given design requirement. Starting with the second half of the 20th century, the industry saw enormous growth in development as well as production numbers of FRPs (5.9 million tonnes in 1999, 8.7 million tonnes in 2011).[7]

Presently, research efforts in this field are mostly concerned with environmental implications regarding the energy intensive production of synthetic fibres and limited recyclability of FRPs in general,[8–10] leading to a push towards plant based fibres and reinforcement materials not generated from petroleum-based sources. At the same time, efforts have been made to improve upon the already high specific strength and modulus of FRPs, enabling lighter and greener solutions, especially compared to metals.[11] More recent advances include hierarchical composite materials, which aim to introduce more structural levels across length scales, resulting in increased optimisation potential and thus improved material properties.[12–14] Inspiration for artificial hierarchical materials can stem from biological materials, such as wood or bone.[15] One of such materials shall be described in more detail subsequently.

1.2. Nacre: structure and mechanical properties

Nacre, also known as mother of pearl, is an iridescent material, forming the inner layer of various mollusc's shells. Despite its high inorganic content of 95 wt% aragonite, a polymorph of $CaCO_3$, the material displays mechanical properties far exceeding those of monolithic aragonite.[16,17] This can be explained by its hierarchical structure. At the microscale, nacre is formed out of platelets approximately 5 µm wide and 200-900 nm thick containing mainly crystalline $CaCO_3$, each surrounded by 10-50 nm of organic mortar, consisting of proteins and polysaccharides.[18] Within this mortar, platelets are aligned alongside the crystallographic [001] direction, resulting in the brick and mortar structure[19], depicted in Figure 1. At the nanoscale, each platelet consists of bridged nanocrystals, embedded within a matrix of organic polymers. The whole assembly is oriented during the biomineralization phase of the organism growing the nacreous layer, resulting in pseudo-single crystal nacre platelets.[20,21]

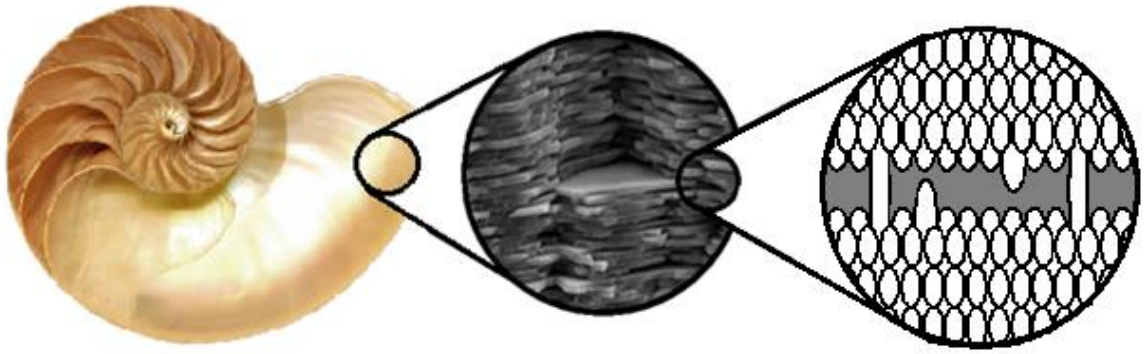

Figure 1: From left to right: nacreous layer on the inside of a Nautilus shell; micrograph of aragonite platelets within the nacre structure; aragonite nanocrystals (white) & interlamellar space with organic mortar (grey).

Despite its high content of inorganic material, nacre features a balance of strength and toughness normally observed in metals and polymers.[22,23] Traditional ceramic materials feature a high modulus at the cost of being brittle, with ceramic composites usually sacrificing strength for reduced brittleness. The well-rounded properties of (hydrated) nacre are enabled by work hardening as a result of pulling apart the aragonite platelets until a macroscopic fracture forms after complete pull-out. In contrast to other composite materials, sliding resistance increases with decreasing platelet interface, leading to gradual pull out across many individual platelets.[19] This unusual behaviour is not yet fully understood, postulated explanations include platelet surface roughness[24], mineral bridges[25,26] and platelet interlocking.[26,27] A visual explanation for the aforementioned mechanisms is shown in Figure 2. Nacre's

remarkable properties have motivated research into production of artificial mimics[28] as well as biomimetic materials inspired by nacre.[29] Efforts to integrate the nacreous structure into a hierarchical composite material shall be described in the next chapter.

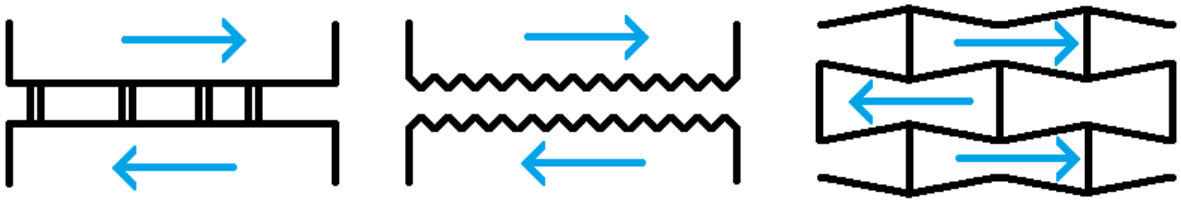

Figure 2: Models for interfacial sliding resistance, from left to right: mineral bridge model; surface roughness model; platelet interlocking model. Arrows represent platelet movement relative to one another.

1.3. Nacre micromimetics in FRPs

One of the major challenges with traditional fibre reinforced composite materials is the dichotomy between high strength coupled with brittle failure or increased toughness at the cost of lower ultimate strength.[30] Because fibre strength is statistically distributed, fibre failure will occur randomly throughout a FRP material once a tensile load is exerted upon it. Once broken, the load previously borne by a given fibre is transferred to neighbouring fibres, without any noticeable macroscopic damage. Further increases in stress are proportional to fibre defect concentration across the specimen. Eventually a local concentration of failed fibres will cause a cascading failure of remaining fibres, resulting in sudden brittle failure of the material.[31] A visual description of the mechanism is presented in Figure 3. Although ways have been described to improve interfacial adhesion[32], resulting in higher strength and brittleness, strategies to improve strength and toughness simultaneously are still needed. Enhanced strength without the need to sacrifice toughness could be achieved in FRPs through employment of toughening mechanisms exhibited by nacre. One such strategy developed by de Luca et al.[33–35] shall be described hereafter.

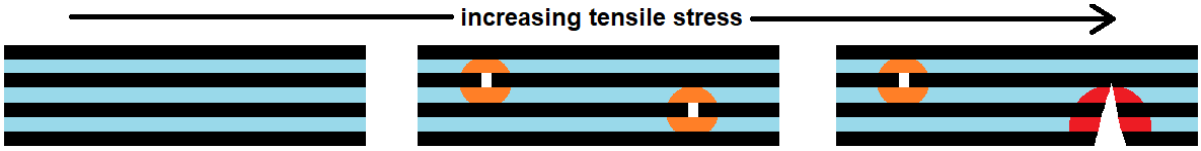

Figure 3: Left: An idealized FRP material under no mechanical stress: fibres are black, matrix is light blue. Middle: tensile stress causes breakage of individual fibres, load transfer to neighbouring fibres depicted in orange, no macroscopic damage. Right: formation of a critical cluster causes cascading and therefore catastrophic failure of the material, visualized in red.

De Luca's design envisions a nanostructured, brick and mortar type interface within a FRP material. Increases in ductility will be achieved through work hardening enabled by the platelet pull out mechanisms described in chapter 1.2. Furthermore, the inorganic "bricks" on a fibre surface should result in crack deflection along the softer "mortar", further delaying eventual fibre failure. Because naturally occurring nacreous platelets display platelet sizes in µm-range and the intended usage being a coating for carbon fibres 7 µm in diameter, a structural analogue an order of magnitude smaller is needed.

1.4. The LDH/PSS system and its deposition onto carbon fibres

The nanometre scaled brick and mortar type structure proposed by de Luca consists of Al/Mg layered double hydroxide (henceforth LDH), a naturally occurring, self organizing, clay-type material and polystyrene sulfonate (henceforth PSS), a water soluble, negatively charged polymer. Carbon fibres are activated using plasma assisted surface oxidation, followed by treatment with 1M $KMnO_4$ to introduce negatively charged groups at the fibre's surface. Activated carbon fibres are coated with an initial layer of positively charged poly(diallyldimethylammonium) chloride (PDDA). The softer PDDA interface was shown to provide better adhesion to the fibre surface. Subsequently, dip-coating is utilized to deposit an LDH/PSS brick and mortar type structure through layer-by-layer deposition. The coating procedure is outlined in Figure 4.

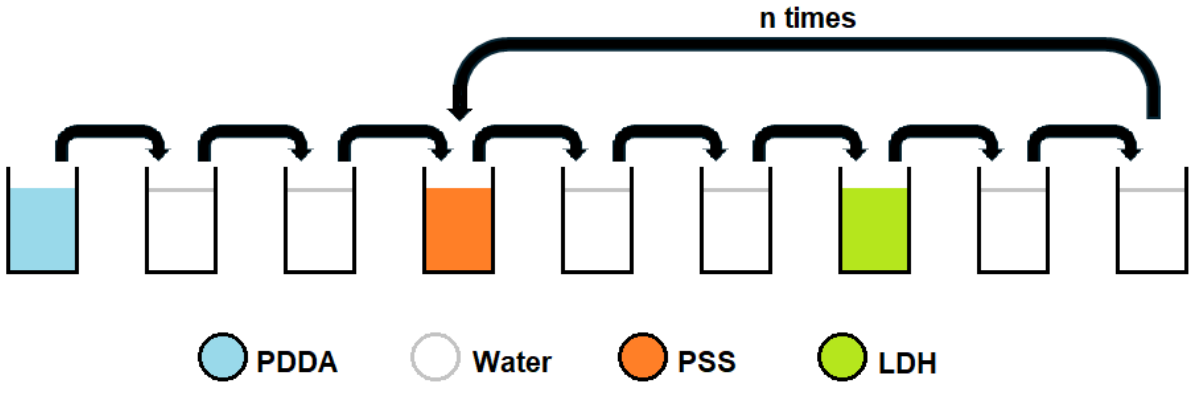

Figure 4: A graphical representation of the process used by de Luca.

The structure of LDHs is fundamentally based on the structure of Brucite [$Mg(OH)_2$]. It consists of divalent metal cations, surrounded in an approximately octahedral manner by hydroxide ions. These octahedrons assemble into an infinite layer by edge sharing. In the case of LDH, 20-33% of divalent metal cations are substituted by trivalent metal cations, resulting in an overall positive charge of the layer, balanced by intercalated anions, alongside water. Therefore, the general formula for the LDH structure is $[M^{II}_{1-x}M^{III}_x(OH)_2]^{x+}[A^{n-}]_{x/n}\cdot yH_2O$.[36] The LDH configuration discussed in this work uses magnesium as divalent and aluminium as trivalent cations. Figure 5 depicts the structure of a LDH layer.

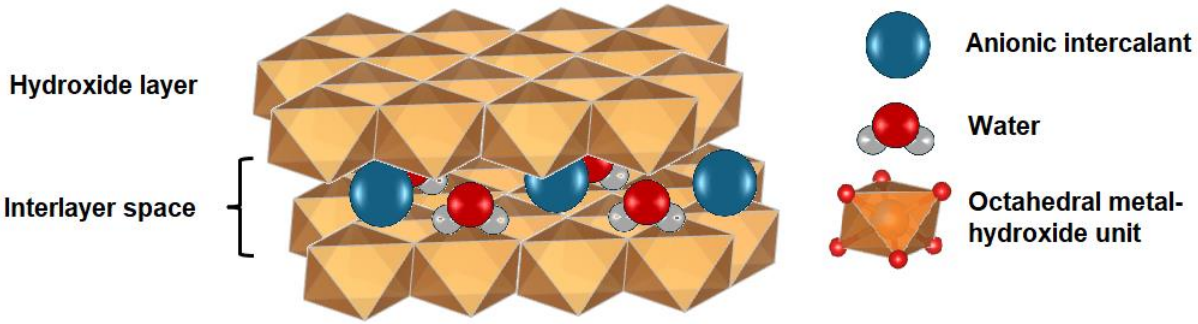

Figure 5: The LDH structure alongside its intercalants.

De Luca was able to prove that a carbon fibre composite interface structured in the aforementioned fashion does indeed lead to improved energy absorption until fracture, alongside higher strain to failure and higher strength. However, dip-coating, due to the manufacturing pipeline being non-continuous, does not scale well with production volume. Therefore, a continuous manufacturing process is needed to achieve production of nacre micromimetic FRPs at scale.

1.5. Electrophoretic deposition for continuous coating of fibres

Electrophoretic deposition (EPD) is an easy, fast and scalable method to deposit particles from a colloidal suspension onto a charged surface. To achieve a coating by means of EPD, a potential must be applied across a colloidal suspension via two electrodes. Deposition will occur on either the anode or cathode, depending on the surface charge of the particle in suspension.[37] The working principle is depicted in Figure 6.

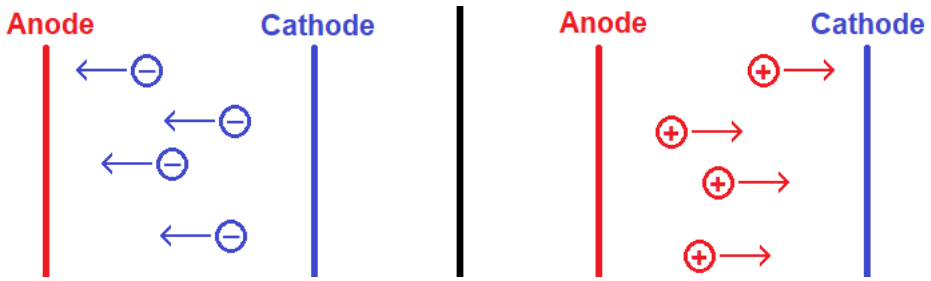

Figure 6: left: anodic EPD; right: cathodic EPD

Deposition yield (w) is dependant upon field strength (E), electrophoretic mobility (μ), mass concentration of particles in suspension (C), permittivity (ε), zeta potential (ζ), viscosity (η) and length, radius of the working electrode (l,a) as well as the radius of the counter electrode (b), according to Avgustinik's law (equation (1)).[38]

$$w = \frac{l*E*\varepsilon*\zeta*C*t}{3\ln\left(\frac{a}{b}\right)*\eta} \quad (1)$$

1.6. Motivation and aim

The goal of this work is the development of a continuous, single step deposition process for a brick-and-mortar type interface on carbon fibres that can be integrated into the production process of carbon fibre/polyetherimide (PEI) composite tapes on the pilot powder impregnation line for composite prepreg production. The following goals must be met for successful completion of aforementioned goal:

- Synthesis of a stable, aqueous, colloidal suspension of LDH nanoparticles of defined particle size and distribution at bench and impregnation line scale.
- Integration of a polymeric species into the LDH suspension for brick-and-mortar assembly.
- Deposit LDH platelets from the colloidal system onto carbon fibres using electrophoretic deposition.
- Integrating the deposition process into the powder impregnation line for production of composite materials with superior mechanical properties compared to control samples.

2. Materials and methods

2.1. Materials

Aluminium nitrate nonahydrate, magnesium nitrate hexahydrate, sodium carbonate, sodium hydroxide, poly(sodium 4-styrenesulfonate) solution (M_W ~ 70,000; 30 wt.% in H_2O) and Cremophor A25 were obtained from Sigma-Aldrich. Unsized carbon fibres (HexTow AS4D) were kindly supplied by Hexcel. Commercial LDH (Pural MG 61 HT) was kindly supplied by Sasol Germany. Polyetherimide (henceforth PEI) powder was obtained from an undisclosed source. Epoxy resin (Prime 20ULV) was obtained form Gurit. Deionized water and 96 vol.% ethanol were obtained from internal sources at the University of Vienna. All chemicals and materials were used without further purification or modification unless specified otherwise.

2.2. Methods

2.2.1. LDH Synthesis

LDH was synthesized by adapting an established coprecipitation method[39] for use at ambient pressure conditions. Solutions of $Al(NO_3)_3$ x 9 H_2O and $Mg(NO_3)_2$ x 6 H_2O in deionized water as well as of NaOH and Na_2CO_3 in deionized water were prepared. One part metal salt solution and four parts NaOH/Na_2CO_3 were mixed and stirred at 350 rpm for 20 min. A 1:2 ratio of M^{III} to M^{II} was chosen to maximize ion substitution in the metal hydroxide layer and maximize layer charge density. The exact composition of solutions used for both big and small-scale approaches are listed in Table 1.

Table 1: reactants used for big-scale and small-scale respectively.

	$Al(NO_3)_3$ x 9 H_2O	$Mg(NO_3)_2$ x 6 H_2O	Na_2CO_3	NaOH
Bench scale	2 mmol	4 mmol	1.2 mmol	12 mmol
	20 mL		80 mL	
Upscaled	27.6 mmol	55.2 mmol	16.7 mmol	165.5 mmol
	280 mL		1100 mL	

The resulting precipitate and its solution were transferred to a centrifuge vessel and washed three times by firstly centrifuging at 10000 rpm for 20 min, followed by discarding the supernatant and resuspending the precipitate in ultrapure water. The

obtained slurry was suspended in ultrapure water and peptized at 110°C bath temperature and ambient pressure under reflux conditions for 24 h. The LDH was stored in suspension at pH 7 as received from reflux treatment to avoid platelet aggregation. Resuspending LDH in water through physical methods, such as sonication is already proven to be problematic due to electrostatic interactions between layers combined with high layer charge density,[40,41] ruling out the usage of commercially available LDH for anything else than comparative qualitative analysis. Any increases in the suspension's pH necessary for stability evaluations were achieved trough addition of 0.01 M NaOH.

A typical bench scale approach resulted in 50 mL of 0.4 wt.% aqueous LDH suspension, as indicated by Xu et al.[39] The process was scaled up to generate 2.5 L of 0.4 wt.% LDH suspension, necessary to perform EPD during production of hierarchical composite tapes using the composite line described in chapter 2.2.5.

2.2.2. In-situ synthesis of LDH

Because of eventual difficulties in creation of a colloidally stable LDH/polymer nanocomposite suspension in water, an attempt was made to circumvent suspension of previously synthesized nanocomposites by growing LDH in situ using electrocoagulation.[42] 400 mL of the metal salt solution described in Chapter 2.2.1 was prepared. A potential of 5 V was applied for times between 5 and 30 min, leading to the cathodic formation of hydroxyl anions, which precipitate with metal cations to form LDH. Potentials over 5 V were not feasible because LDH growth was disturbed by gas formation from electrolysis. The anodic formation of oxygen and solvated cations from anode material necessitates the usage of a sacrificial anode. This method was only employed at bench scale, as anode degradation would lead to the destruction of the graphite electrode plates employed at the scaled setup.

2.2.3. LDH characterisation

The morphology, particle size and particle size distribution of LDH particles were characterized using scanning electron microscopy (SEM) images of platelets obtained from drying 0.4 wt.% LDH suspension, diluted by a factor of 500 on aluminium foil. A conductive gold coating was applied by physical vapour deposition to facilitate dissipation of charge build up. A Zeiss Supra 55 VP SEM unit with an accelerating voltage of 5 kV and magnifications of 18.4 and 69.6 kx were utilized. The particle size

distribution was calculated from 465 analysed particles using imageJ software. The results were plotted in a histogram and fitted with a lognormal distribution curve using OriginPro 2023 software. The data obtained was compared with distribution data obtained by performing dynamic light scattering (DLS) on 0.4 wt.% LDH suspension using a Malvern Zetasizer Nano.

X-ray diffractometry (XRD) was carried out using a Malvern Empyrean to determine overall crystallinity and adherence to the theoretical unit cell. Samples were prepared by drying LDH filtered from suspension at 100°C overnight. Dried LDH was powdered using a mortar and pestle. A scan range of 7-100°2θ was employed. The obtained diffractogram was compared to a calculated pattern of a theoretic LDH unit cell.

A Bruker Tensor II infrared (IR) spectrometer was used to obtain spectrograms of dried and powdered LDH samples to determine the chemical structure of the sample. Measurement range was set from 400-4000 cm^{-1}. Spectra of synthesized LDH, commercially available LDH and LDH deposited on an electrode surface by means of EPD were obtained.

Thermogravimetric analysis was performed using a TA instruments Discovery TGA. Synthesized and commercially obtained LDH was examined to determine relative weight loss over temperature by physical and chemical processes such as water desorption and thermally initiated dehydroxylation and decomposition reactions. Temperature was increased by 10°C/min from 40°C to 110°C, followed by a ten-minute isotherm at 110°C and a subsequent increase by 10°C/min to 800°C. Measurements were conducted under atmospheric conditions.

The synthesized LDH suspensions were characterized by their zeta potential to determine particle surface charge at the shear plane and therefore their ability to form a colloidal suspension, using a Malvern Zetasizer Nano. Sedimentation rates of suspensions were investigated using a Krüss K100 equipped with a sedimentation probe. Suspensions were stirred for 5 min until the immediate beginning of testing. Surface detection speed was set to 50 mm/min, immersion speed was set to 100 mm/min, measurement time was set to 300 s. The last 100 s of each measurement were linearly fitted, the resulting function's slope was recorded as sedimentation. A schematic to illustrate the process is presented in Figure 7.

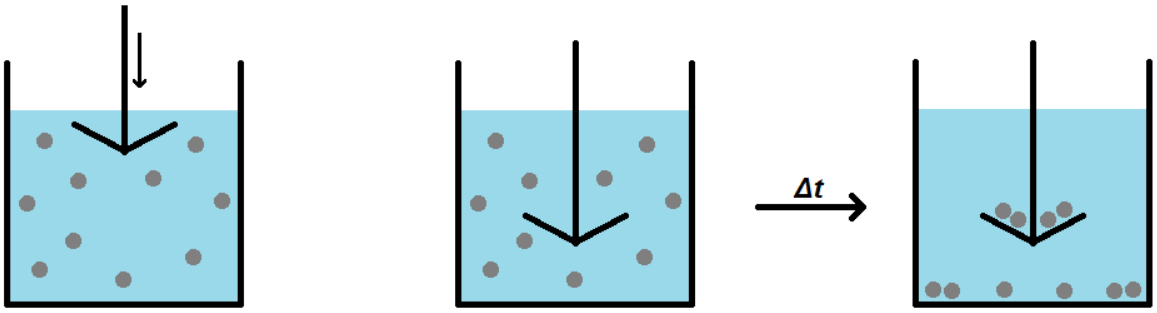

Figure 7: left: after surface detection, the concave sedimentation probe is immersed within the examined suspension. Middle: upon complete immersion of the measurement probe, mass data acquisition will commence. Right: over time, any given unstable suspension will result in an increase of recorded mass over time.

2.2.4. Electrophoretic deposition (EPD)

EPD experiments at laboratory scale were conducted using a cell assembly consisting of 400 mL 0.1 wt.% LDH suspension (0.4 wt.% suspension as synthesized, 300 mL water), fused deposition modelled (FDM) polylactic acid support structures for either graphite foil or aluminium foil anodes and carbon fibre tow cathodes as substrate for deposition. Preliminary testing was also performed with 72 vol.% ethanolic LDH suspension (0.4 wt.% LDH suspension as synthesized, 300 mL 96 vol.% ethanol). In contrast to the aqueous deposition, EPD from an ethanolic suspension was configured as anodic deposition, since carbonate is less soluble in ethanol and will not desorb as readily from particles during EPD. An Electro-Automatik EA-PS 3065-05 B linear DC power supply was used as power source. The exact setup used is depicted in Figure 8. The deposition rate was determined gravimetrically by performing three subsequent EPD cycles using the same suspension. After each deposition, five 2 mL fractions were isolated and dried. The LDH weight fractions after depositions were calculated using residual masses of the isolated samples, resulting in change of LDH weight fraction in suspension over completed EPD cycles.

The benchtop setup was scaled to a volume of 11 L to facilitate EPD at the K03 composite line. Horizontally oriented graphite electrodes were used in place of graphite foil, the beaker was replaced by a polymethyl methacrylate (PMMA) vessel with pre-installed, FDM printed structures to facilitate the guidance of the carbon fibre (CF) tow and mounting of the electrodes. The same power supply as with the small-scale setup was used. Only aqueous cathodic deposition was performed. A diagram of the setup alongside a picture is depicted in Figure 9.

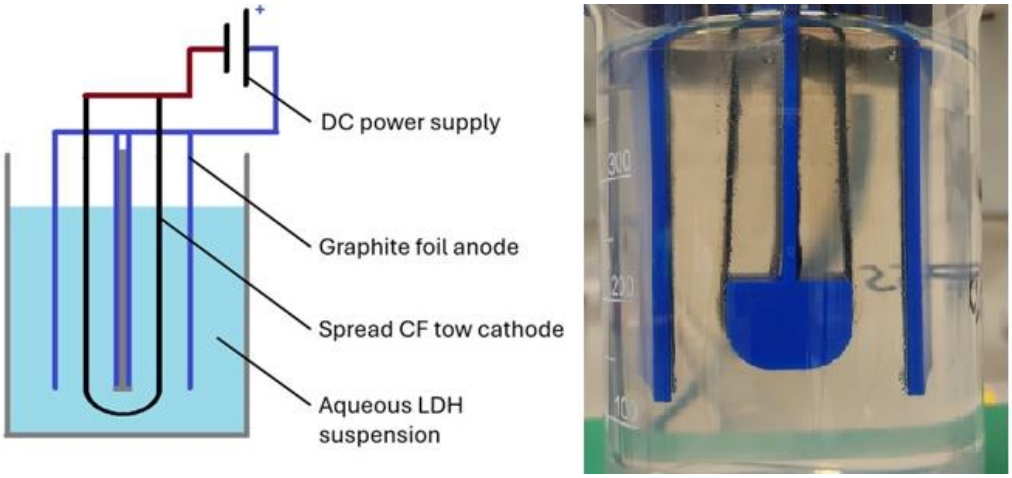

Figure 8: Diagram (left) and picture (right) of the laboratory scale setup used for aqueous deposition.

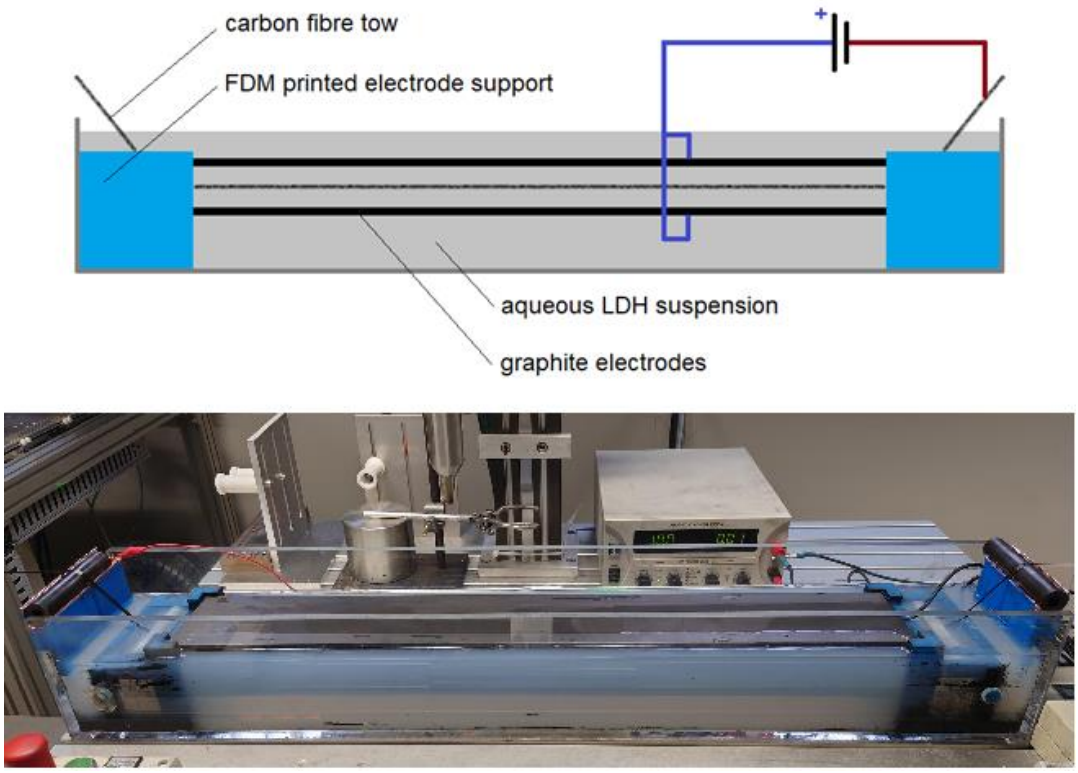

Figure 9: Top: Diagram of the EPD cell used for experiments involving the K03 composite line. Bottom: side view of the EPD cell used for experiments involving the K03 composite line.

2.2.5. Manufacturing of composite tapes and laminates

The k03 powder impregnation line was used for manufacturing of hierarchical composite tapes. The line was configured as shown in Figure 10. Consequently, the fibres were first subjected to EPD, followed by PEI resin infiltration from a suspension containing 4 wt.% PEI, 2 wt.% ethanol and 4 wt.% Chremophore A25 with respect to the suspension's weight. Removal of water was facilitated by two IR heating elements

(100 and 120°C), followed by incorporation and polycondensation of PEI resin through shear pins heated at 350°C. The produced tape was cut into 20 cm long parts, which were sorted by their width, fibre weight fraction (FWF) and fibre volume fraction (FVF). FWF was determined using equation (2), FVF was determined using equations (3) and (4). Only tapes 9-10 mm wide, with a FWF of 64 ± 5 % were chosen for hot press consolidation into laminates. Consolidation was performed on 35 prepreg plies in a steel mould equipped with release film (UBE Upilex). Consolidation was performed in three stages: 300°C at contact pressure for 10 min, followed by 300°C at 1-2 t_f for 10 min, followed by 100°C at 0.5-1 t_f for 10 min in a different hot press for annealing.

$$FWF = \frac{\lambda_{CF}*0.2}{m_{prepreg}} * 100 \quad (2)$$

$$\rho_{prepreg} = \frac{(\lambda_{CF}*0.2*\rho_{CF})+(m_{prepreg}-\lambda_{CF}*0.2)*\rho_{PEI}}{m_{prepreg}} \quad (3)$$

$$FVF = \frac{\rho_{prepreg}*FWF}{\rho_{CF}} \quad (4)$$

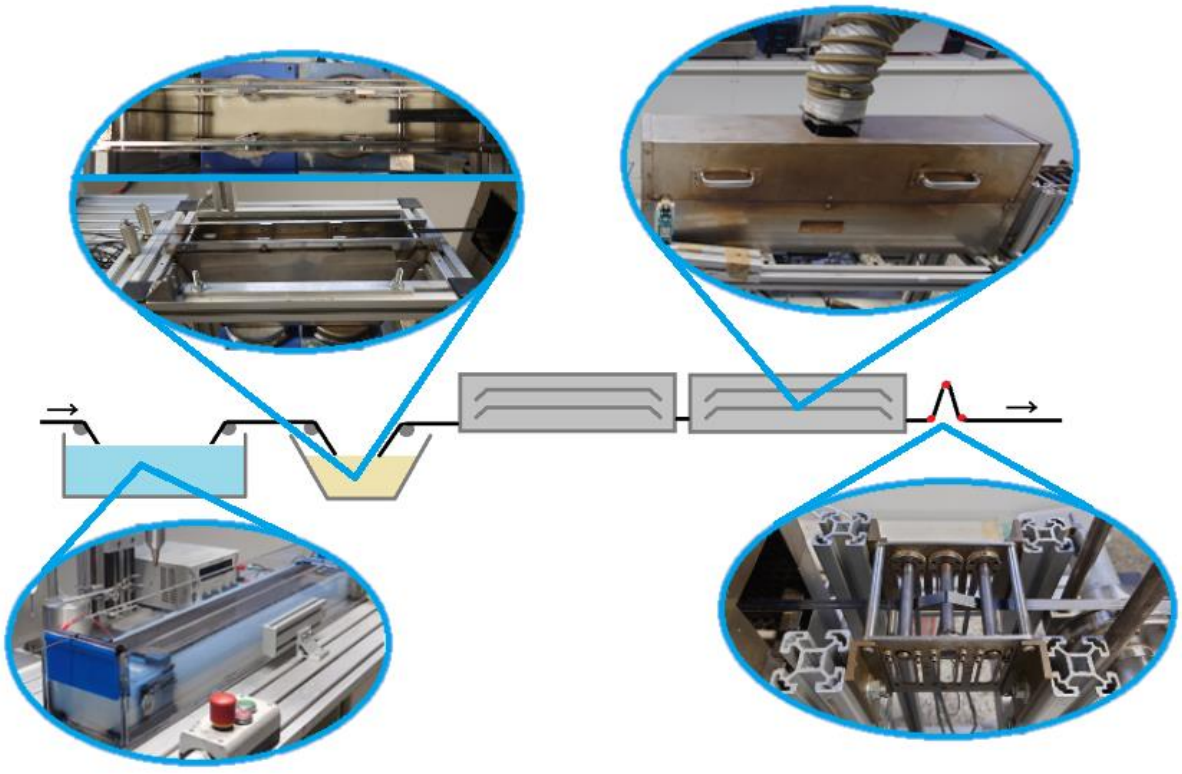

Figure 10: Schematic of the k03 composite line used for scaled manufacturing, alongside photos of individual line components, from left to right: EPD bath, PEI infiltration bath, IR furnaces, heated shear pins.

2.2.6. Characterisation of coated carbon fibres

The morphology, uniformity and particle size distribution of LDH platelets deposited on carbon fibres were examined using SEM micrographs. Analysis of particle size and distribution were performed using imageJ and Origin 2023b software. The underestimation of platelet size due to fibre curvature was compensated by factoring in the ratio of projected (measured) and real (calculated) platelet size, averaged over the investigated distance from the centre of the fibre. A graphical representation of the compensation method is depicted in Figure 11.

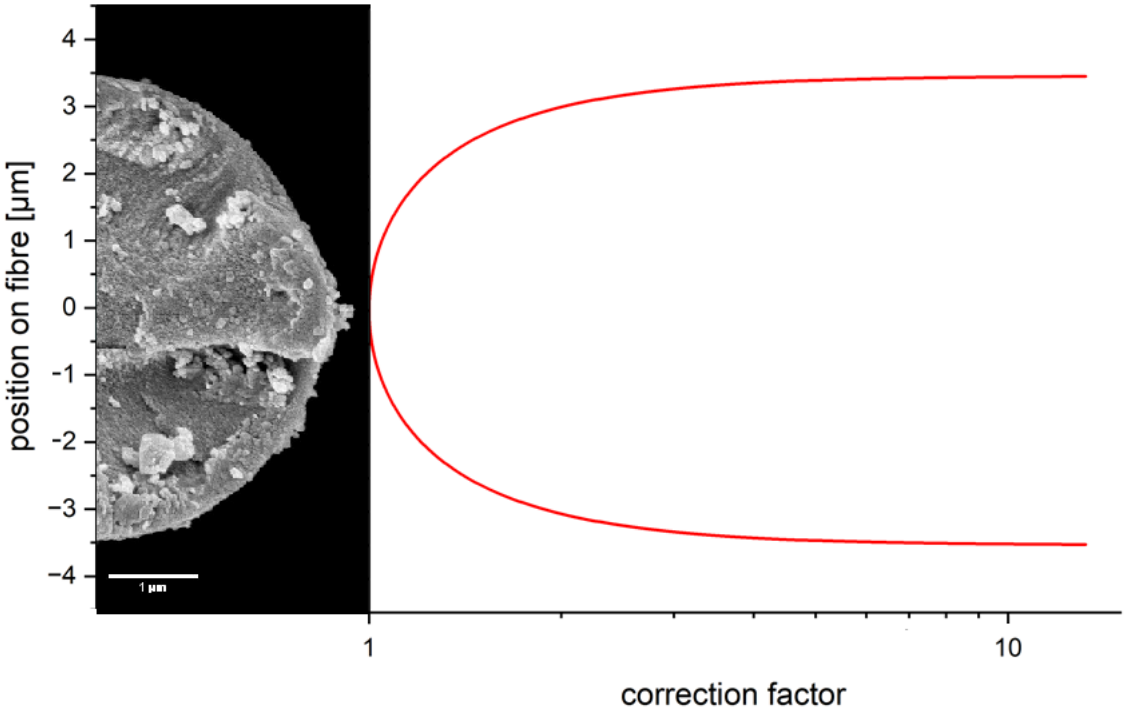

Figure 11: Graphical representation of the factor between projected and real particle, dependant upon distance from fibre centre.

X-ray photoelectron spectroscopy (XPS) elemental analysis was performed using a ThermoScientific Nexsa on samples manufactured using the k03 composite line. Samples included uncoated carbon fibres and fibres subjected to EPD with potentials of 0 V, 10 V, 20 V, and 30 V respectively. C1s, O1s, Mg1s, Al2p and N1s binding energy peaks were investigated.

2.2.7. Characterisation of composite laminates

Fibre alignment was determined using method described by Yurgartis.[43] Sections of CF/LDH/PEI unidirectional composite laminate were embedded in epoxy (PRIME 20ULV, Gurit). Samples were cut at a plane cut angle of φ_{PC} = 5° relative to fibre direction, ground, polished and examined using a Leica DM2700M microscope. The angle ω_i of any given fibre relative to the sectioning plane was determined by using equation (5). Fibre misalignment θ is then determined from the median ω of the set of all ω_i using equation (6). The median was chosen over the mean, because a bias against fibres approaching $\theta_i = \varphi_{PC}$ is inherent to the method, caused by the microscope's limited field of view. To achieve a representative value, 10 random fibres from 20 images each were evaluated.

$$\omega_i = sin^{-1}\frac{d}{l} \tag{5}$$

$$\theta = \omega - \varphi_{PC} \tag{6}$$

Void content was determined by first determining composite density using gas pycnometry (Micromeritics AccuPyc II 1340). Ten measurements of the same sample were performed. Composite void volume ratio could then be determined using Equation (7).

$$V_v = 1 - \frac{\rho_c}{FVF*\rho_{CF}+(1-FVF)*\rho_M} \tag{7}$$

To determine possible negative effects of LDH at the interface, the apparent interlaminar shear strength (ILSS, τ_M) was determined using the short beam test method (ISO 14130). Five specimens measuring 20x10x2 mm were tested. Specimens were placed on two parallel, horizontally mounted, cylindrical support members, (1,2) plane horizontal, fibre direction parallel to support members radius. Force was applied through a loading member midway between the supports. ILSS was determined following equation (8).

$$\tau_M = 0.75 * \frac{F_M}{bh} \tag{8}$$

F_M is the load at point of failure, b and h are height and width of the specimen. ILSS data of CF/PEI laminate was used as control.

3. Results

3.1. LDH platelets

3.1.1. Particle morphology, size and size distribution

SEM micrographs of synthesized LDH powder dried from suspension show both individual platelets as well as LDH agglomerates, a range of platelet dimensions and shapes ranging from rounded to hexagonal, as shown in Figure 12.

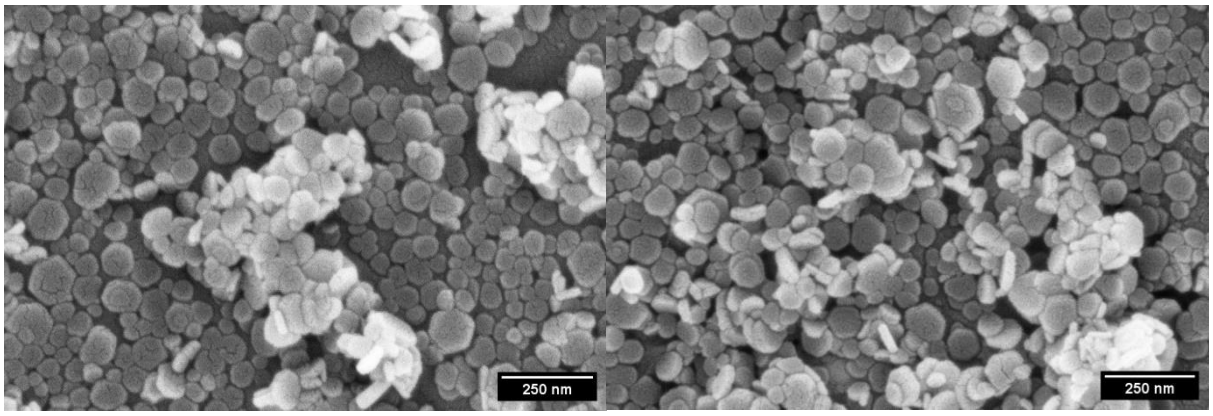

Figure 12: SEM micrographs of synthesized LDH particles (24 h reflux treatment) deposited on aluminium foil.

Overall mean particle size was found to be dependent upon reflux time after synthesis; longer reflux times resulting in increased size and reduced size distribution. Particle size data obtained from DLS and SEM yield different results, as agglomerates were excluded from evaluation in SEM. Both methods and the dependency of particle size to reflux time are depicted in Figure 13.

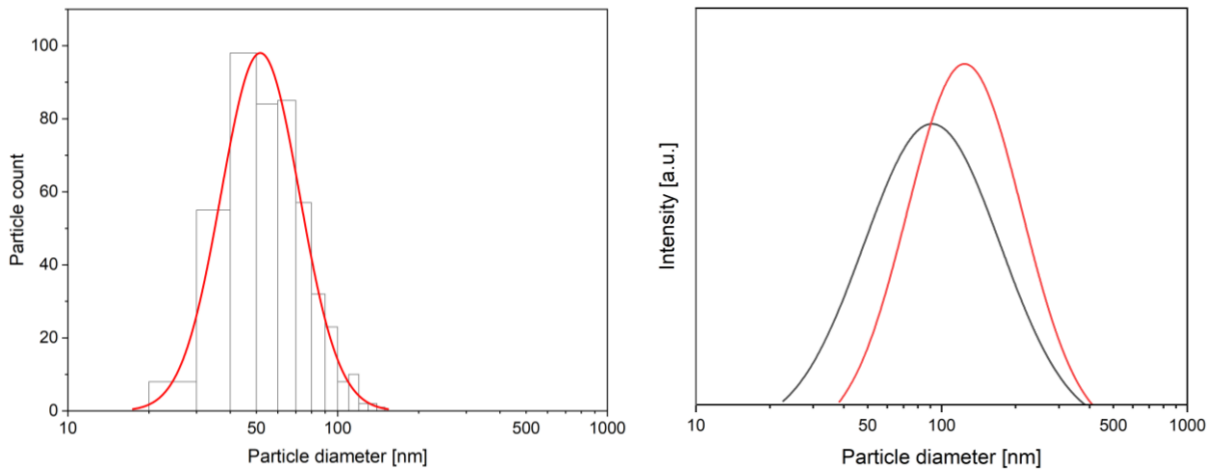

Figure 13: left: histogram of particle size in SEM micrographs depicted in Figure 12. Right: Particle size of samples with 2h reflux time (black) and 24h reflux time (red), measured by DLS.

3.1.2. Crystallinity

Powder diffraction patterns of synthesized LDH dried from suspension and the pattern calculated using the theoretical LDH unit cell were found to be in agreement. Synthesized LDH displays crystallinity, with broader peaks at 35, 40 and 47° 2θ corresponding to reflection planes (012), (015), and (018), respectively; suggesting parallel displacement of Brucite layers in the (003) plane relative to one another. The diffraction pattern is depicted in Figure 14, alongside the corresponding unit cell.

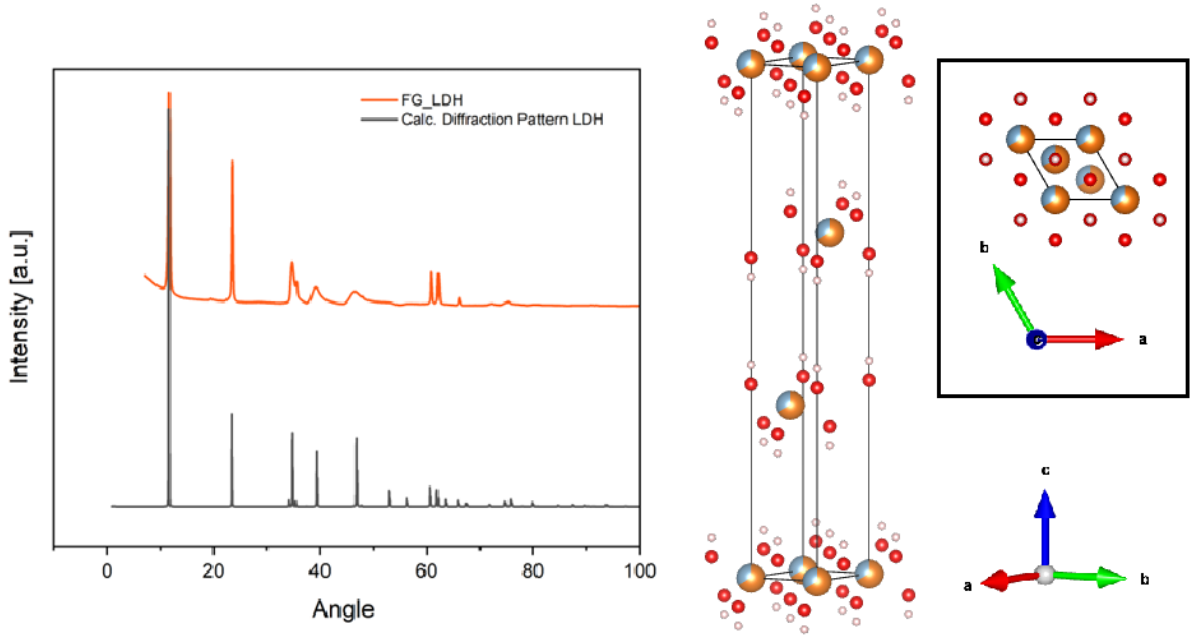

Figure 14: left: measured and calculated powder diffraction pattern of LDH. Right: unit cell of LDH. Bonds and intercalated carbonate anions were omitted for visual reasons. Hydrogen atoms are depicted in white, oxygen atoms in red, metals in silver/orange. Unit cell and calculated pattern were obtained from Crystallography open database (COD ID: 9009272).

3.1.3. Spectroscopic results

FTIR spectra of synthesized and commercially obtained LDH powder were nearly identical. LDH recovered after EPD also displayed a similar spectrum, albeit with less intensive peaks due to the small sample volume. Potential alterations in chemical structure due to EPD were not observable in FTIR. Bands observed below 1000 cm^{-1} correspond to metal-oxygen-metal vibrations from the brucite layer as well as C-O vibrations from intercalated carbonate. The band at 1350 cm^{-1} denotes asymmetric CO_3^{2-} bond stretching, also stemming from intercalated carbonate. The broad band above 3000 cm^{-1} can be attributed to O-H bond stretching. The discussed spectra are depicted in Figure 15.

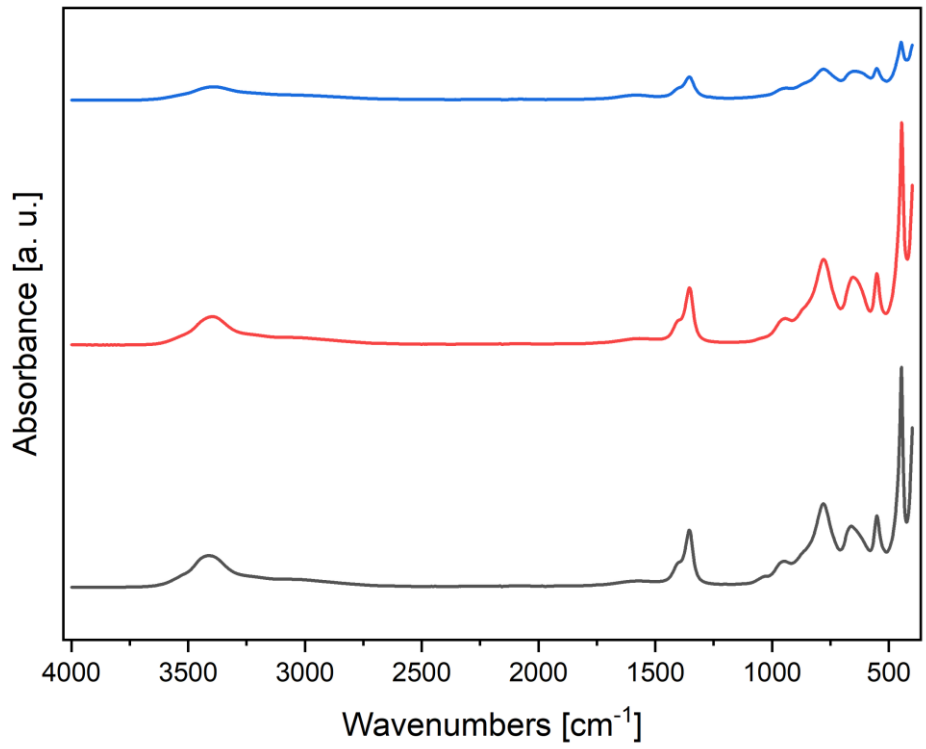

Figure 15: black: LDH as synthesized, red: commercially obtained LDH (Pural), blue: synthesized LDH recovered from working electrode after EPD

3.1.4. Thermal decomposition behaviour

Thermograms of synthesized (FG_LDH) and commercially obtained LDH (Pural) shows desorption of intercalated water up until approx. 220°C. Upon further heating, oxidation and subsequent elimination of intercalated carbonate anions as well as the oxidation of the metal hydroxide layers into metal oxide leads to the collapse of the layered LDH structure into LDO (layered double oxide). The commercially obtained LDH retains mass longer due to its larger and more agglomerated platelets affecting evaporation and deintercalation kinetics compared to synthesized LDH. The thermal decomposition behaviour of LDH described here is in agreement with data from literature.[44,45] The data as discussed is depicted in Figure 16. Furthermore, measured (A) and theoretical mass retention (B) - not accounting for crystal water - as calculated according to equations (9) and (10) are in agreement, supporting the claimed formation of LDO.

$$A(Pural) = \frac{0.57}{0.87*0.01} = 65.5\% \quad (9)$$

$$B = \frac{M(Mg_{0.66}Al_{0.33}O_{1.17})}{M([Mg_{0.66}Al_{0.33}(OH_2)]^{0.33}[CO_3^{2-}]_{0.16})*0.01} = 63.7\% \quad (10)$$

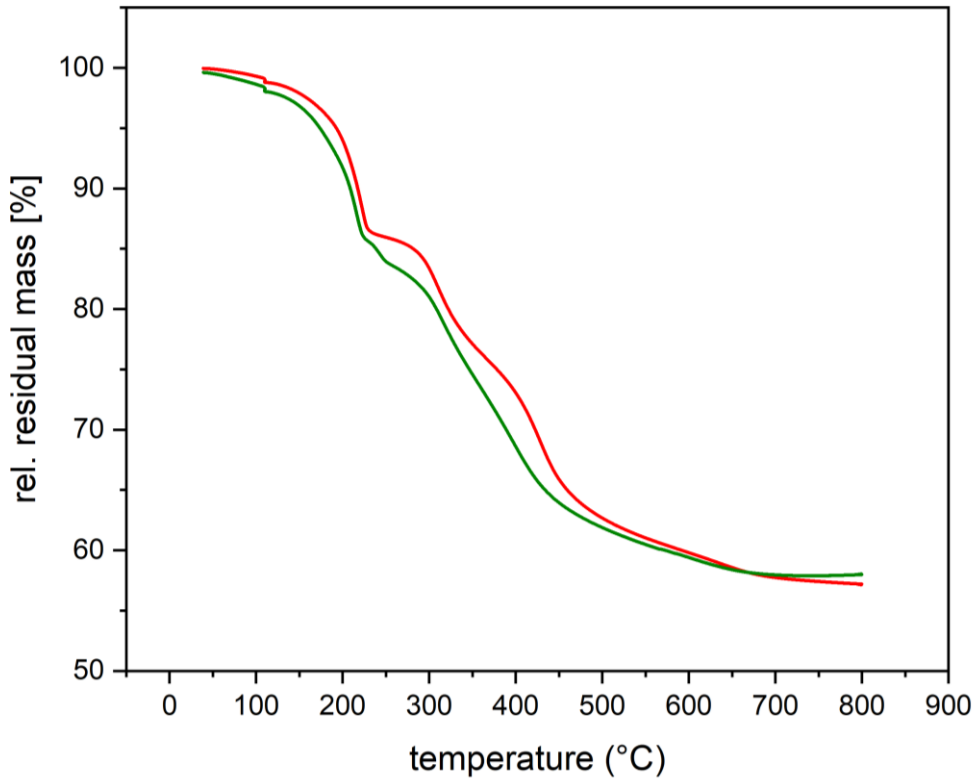

Figure 16: TGA data for synthesized (green) and commercially obtained LDH (red).

3.2. LDH suspension

LDH suspensions as received from synthesis displayed ζ-potentials of around 40 mV. Therefore, they can be considered stable. EPD was not found to have a measurable influence on suspension stability. However, instability of suspensions is observed at pH 8 and above, as well as upon addition of 0.04 wt.% PSS, inferable from decreased ζ-potential and increased aggregate size. Increases in anion concentration result in a degree of surface charge neutralisation and thus significant decreases in ζ-potential, loss of colloidal stability and aggregation. Aggregate size and ζ-potential data is presented in Table 2.

No correlation between EPD and sedimentation time could be established, as no significant difference compared to control (water) can be observed. Sedimentation rate measurements showed reduced short-term stability of suspensions at and above pH 8. Addition of 0.04 wt.% PSS led to immediate precipitation outside of the measuring range of the used instrument, because initiation time of a given sedimentation experiment was longer than the precipitation time of LDH/PSS samples. Sedimentation rates at different pH levels are presented in Table 3.

Because the formation of a LDH/polyanion nanocomposite platelet suspension stable enough for EPD could not be accomplished, deposition experiments were conducted with as synthesized LDH featuring intercalated carbonate anions.

Table 2: agglomeration size and Zeta potential of LDH suspensions at different pH and with added PSS. Samples are pH 7 unless specified otherwise.

Sample	**ζ-potential [mV]**			**Aggregate size DLS [nm]**		
0.4 wt.% LDH	39.0	41.8	40.2	112	112	110
0.1 wt.% LDH, after EPD	38.9	39.1	40.7	114	112	112
0.4 wt.% LDH, pH 8	10.0	10.9	11.1	4460	4600	2130
0.4 wt.% LDH, pH 9	7.0	7.5	7.4	4360	3950	2180
0.4 wt.% LDH, 0.04 wt% PSS	14.9	14.8	14.4	687	3750	4490

Table 3: sedimentation rates of LDH suspensions at different pH values and after being used for EPD.

Sample	**Sedimentation rate [mg/min]**			
Water	0.111	0.188	0.101	0.061
0.1 wt.% LDH, pH 7	0.134	0.150	0.109	0.127
0.1 wt.% LDH, pH 7, after EPD	0.117	0.093	0.049	0.029
0.1 wt.% LDH, pH 8	0.191	0.159	0.153	
0.1 wt.% LDH, pH9	0.419	0.150	0.353	

3.3. LDH-coating of carbon fibres

3.3.1. Electrophoretic deposition

EPD was carried out at bench scale with potentials ranging from 5 V to 15 V and over timeframes between 5 and 60 min. In aqueous suspension, predominately single layer deposition of individual platelets and agglomerates was observed. Macroscopic LDH deposition could not be observed under any conditions in aqueous suspension. Amount of deposited LDH was not dependent upon deposition time and/or potential, since any additionally deposited material was shed upon removal of the working electrode from suspension. Accordingly, one EPD cycle resulted in LDH consumption close to the limit of quantification of the chosen method, as depicted in Figure 17. To coat one meter of carbon fibre tow would require approximately 0.05 g of suspended particles. This would correspond to a LDH layer thickness of 92 nm, if a densely packed layer and ρ(LDH) = ρ(Hydrotalcite)[46] = 2.06 g/cm³ are assumed.

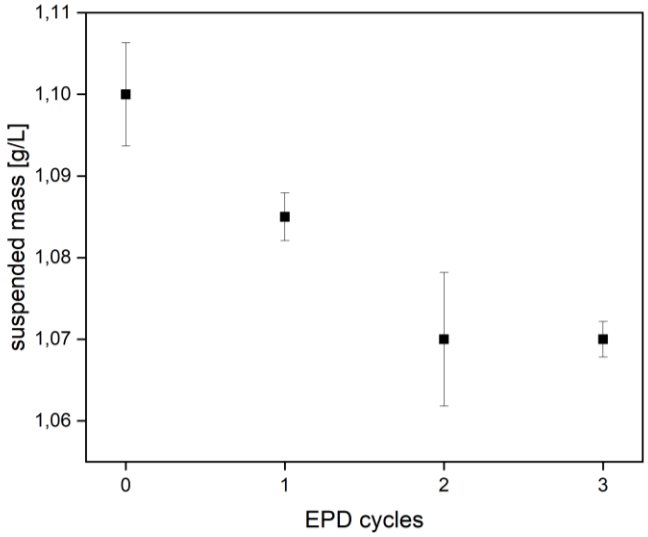

Figure 17: LDH usage per EPD cycle. One cycle equates to 20 cm of coated carbon fibres.

SEM micrographs of coated carbon fibres display deposition of platelets mostly smaller than 100 nm in diameter, alongside aggregates. Size distribution analysis shows no significant difference in particle size and distribution compared to particles isolated directly from suspension. A size histogram alongside the corresponding SEM micrograph is depicted in Figure 18. Evidence of an even, single layer coating can be seen on micrographs depicted in Figure 19. Samples coated during production of composite tapes at the powder impregnation line displayed uncoated areas not observed on samples produced at bench scale, likely due to frictional stresses exerted by the composite line itself. This comparison can be made between Figures 19 (right) and 20 (right).

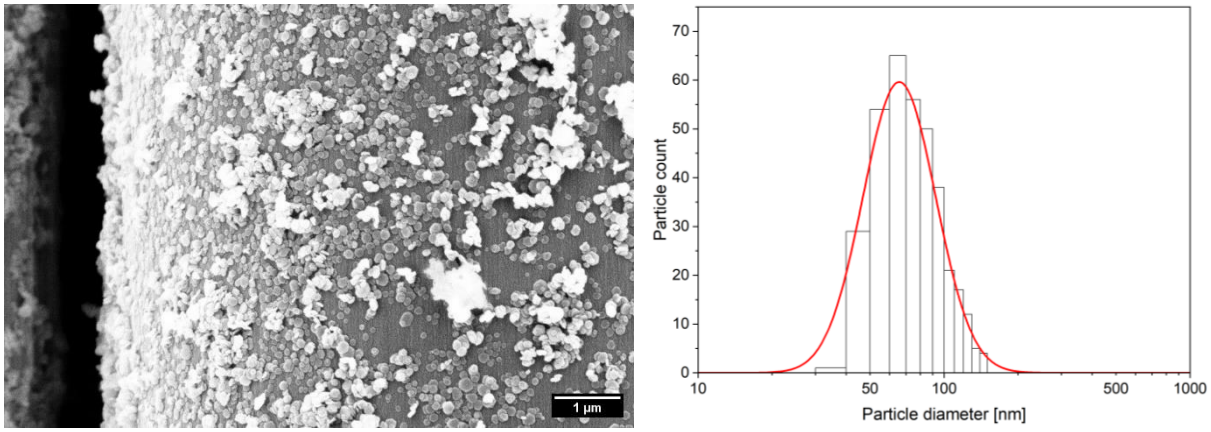

Figure 18: left: particles deposited on a carbon fibre using the scaled setup. Right: particle size distribution of particles located up to 1.3 and -1.6 µm away from the centre of the fibre. Accordingly, particle size was adjusted by factor 1.033.

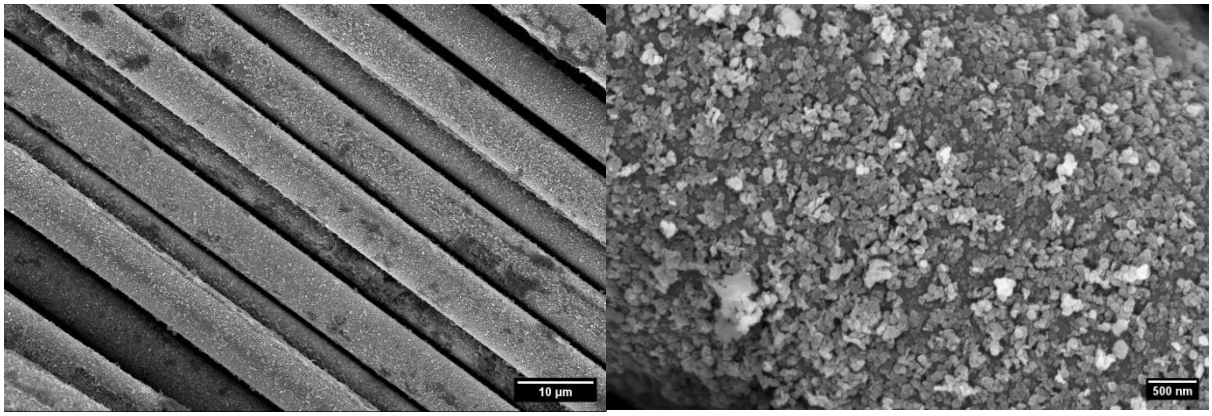

Figure 19: SEM micrographs of samples produced at bench scale (5 min, 5 V, 0 A), displaying an even monolayer LDH coating on carbon fibres.

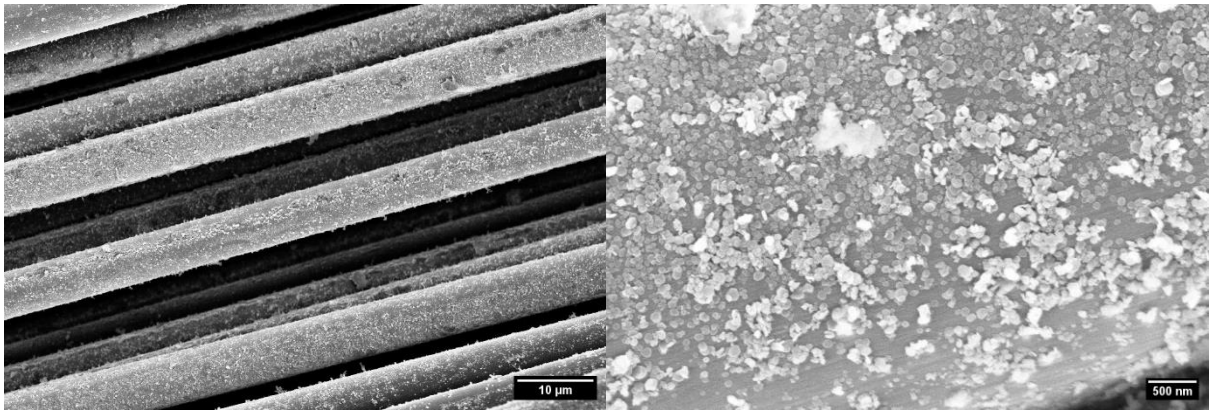

Figure 20: SEM micrographs of samples produced at the k03 composite line (line speed: 0.6 m/min, 30 V, 0.03 A). The coating quality is influenced by manufacturing conditions, coated fibres are being subjected to abrasive conditions during bends under tension.

In contrast to EPD from an aqueous suspension, EPD from an ethanolic suspension resulted in macroscopic LDH deposition (Figure 21). ζ-potential of the used suspension was measured at -5.1 mV, due to lower anion activity in the less polar, ethanolic suspension.

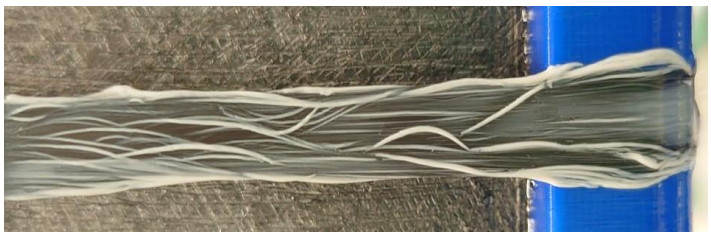

Figure 21: Macroscopic electrophoretic deposition of LDH from 72 vol% ethanolic suspension.

X-ray photoelectron spectroscopy of samples prepared at the k03 composite line show an improvement in coating quality with the usage of EPD compared to pure dip coating. Coating quality is shown to not be dependant upon magnitude of applied potential, however, the sample size presented here is insufficient for a definitive conclusion. Low coating density can be explained by abrasions during production at the k03 composite line. Elemental analysis results are presented in Table 4. One datapoint per sample and element was obtained due to time constraints.

Table 4: XPS elemental analysis of samples produced at the k03 composite line, alongside pristine carbon fibres as control.

Sample	**Analytes [%]**				
	C	O	Mg	Al	N
CF control	94.1	3.30			2.64
CF dipping	69.7	20.4	4.76	3.42	1.81
EPD 10 V	59.1	27.8	6.78	4.60	1.71
EPD 20 V	62.7	25.1	6.30	4.17	1.69
EPD 30 V	53.0	32.0	8.12	5.31	1.54

3.3.2. LDH coatings produced by electrocoagulation

In contrast to coatings produced by EPD, in-situ growth of LDH enabled the growth of multilayer LDH formations in an aqueous environment, as shown in Figure 22. Grown crystallites displayed increased platelet size, increased aspect ratio and stronger adherence to a hexagonal shape compared to platelets produced by coprecipitation. Two distinct growth mechanisms can be observed. Close to fibre surface, crystallites grow normal to fibre surface in a sand rose like formation, likely to minimize for anion concentration over distance to cathode. Sand rose layer thickness was found to be dependant upon deposition time, evident from different deposition times depicted in Figure 23. A second layer was observed on top of the sand rose formation on some fibres, in form of platelets stacked parallel to fibre surface, depicted in Figure 25. The horizontally stacked layer was found on fibres independent of deposition time, distance from the fibre surface and therefore thickness of the sand rose layer, as observable on Figure 24 left and Figure 25: thickness and platelet size of the sand rose layer changes with deposition time, the horizontally stacked layer is present on both samples. Therefore, the formation of the horizontally stacked layer is likely formed upon the removal of potential.

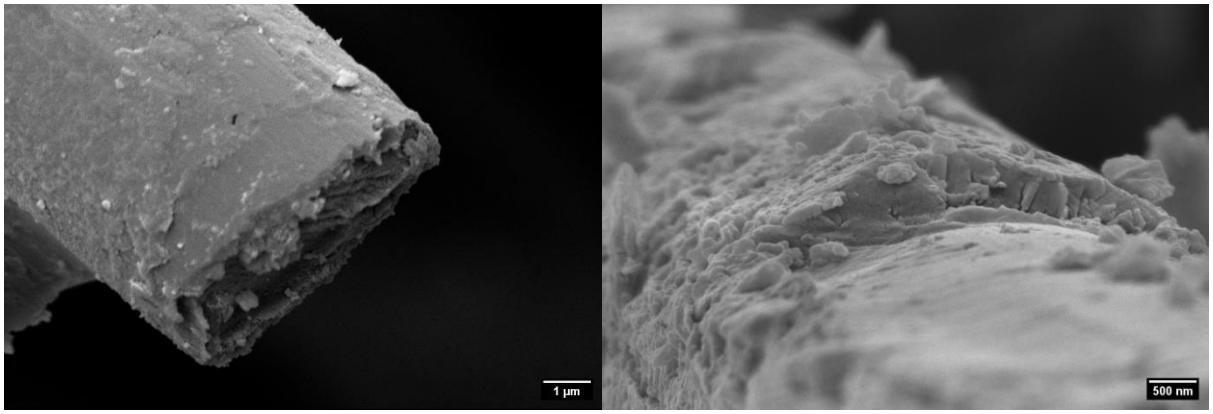

Figure 22: Electrocoagulation can form thicker LDH coatings in aqueous environments than EPD.

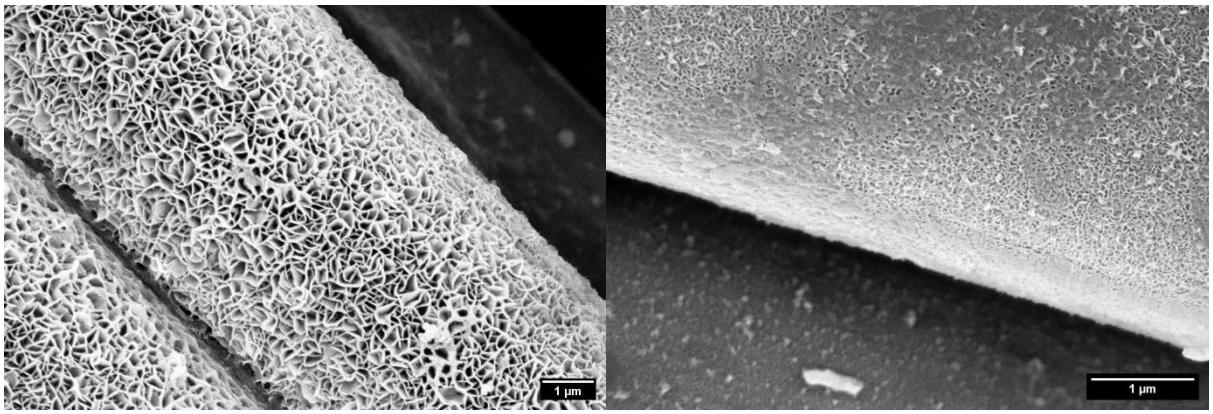

Figure 23: Sand rose formations of different platelet size grown on carbon fibres. Left: 5 V, 0.18 A, 30 min. Right: 5 V, 0.18 A, 5 min

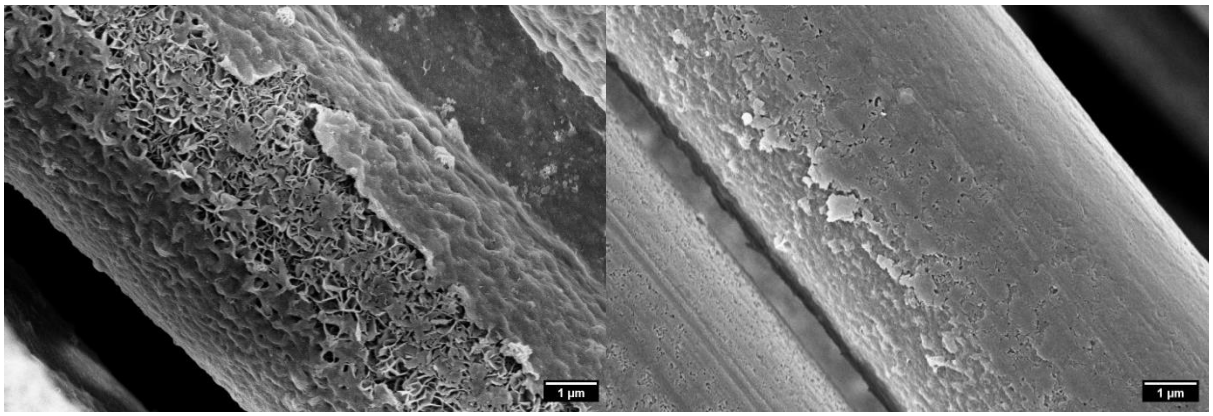

Figure 24: left: sand rose layer on a carbon fibre, incompletely covered by horizontally stacked LDH. Right: fully developed layer of horizontally stacked, in situ grown LDH. Both coatings were grown at 5 V, 0.18 A, 30 min.

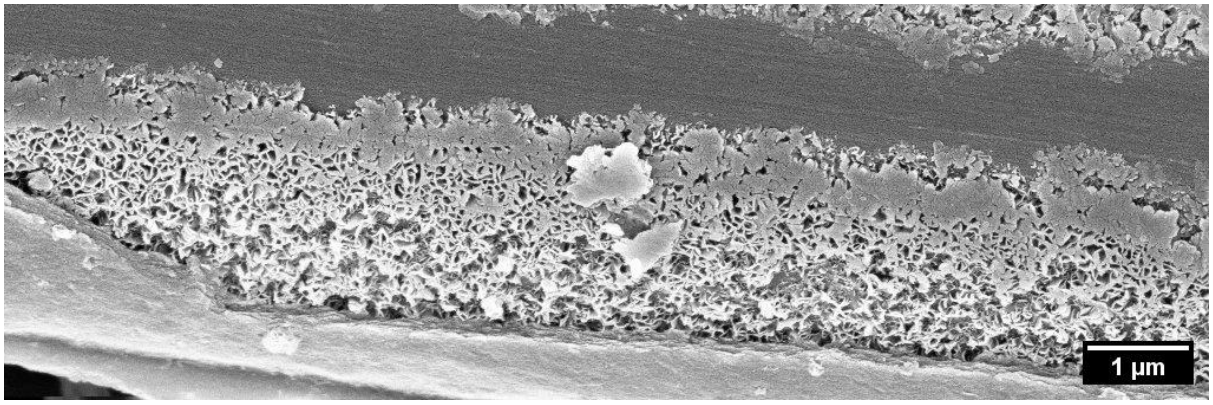

Figure 25: SEM micrograph displaying bare carbon fibre surface (top), sand rose layer (middle) and horizontally stacked top layer of LDH. Cross section is likely the result of a neighbouring fibre's imprint. Experimental conditions: 5 V, 0.18 A, 5 min.

3.4. Production of CF/LDH/PEI composites

3.4.1. Production of composite tapes

A total of 72.6 m of composite tape were produced over three production runs at the powder impregnation line. The tape was sectioned into parts measuring 20 cm in length. 55 out of 115 sections from the first run, 19 out of 135 sections from the second run and 0 out of 113 sections from the third run were meeting the hot press consolidation requirements of width ranging from 9-10 mm and FVF ranging from 53-63 %. In total, tape yield for consolidation was calculated at 20.4 %. The high variance in tape quality is potentially caused by the slow line speed of 0.6 m/min, necessitated by EPD time requirements. A graphical representation of the results of the first and second run is depicted in Figure 26.

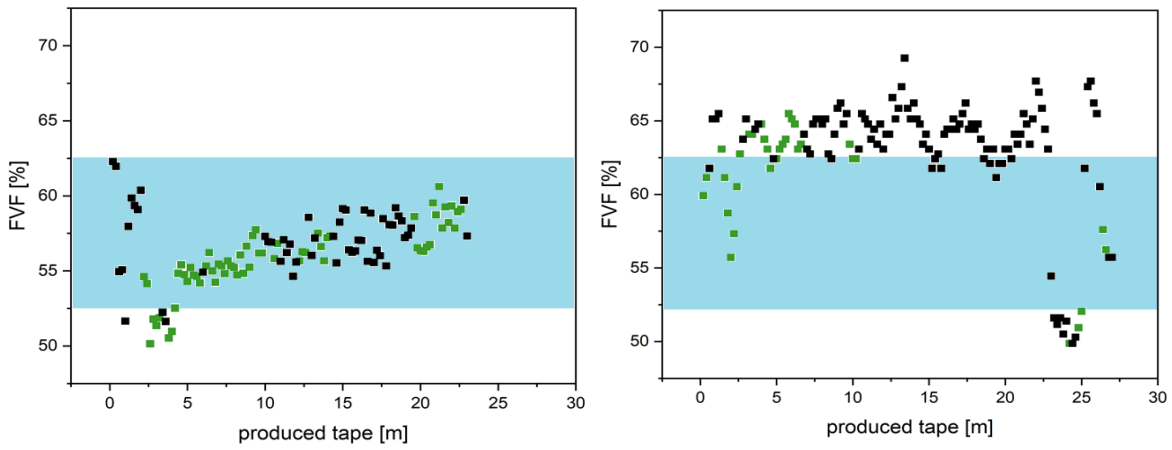

Figure 26: first (left) and second (right) production run of CF/LDH/PEI composite tapes at the k03 composite line. Green dots represent tape sections which meet the width requirement for consolidation. The blue section represents the FVF requirement for consolidation.

3.4.2. Laminate: fibre alignment and void volume

The distribution analysis of fibre misalignment showed fibre angles from -4° to 11°. The mean was determined at 0.65° ± 2.4°. 77.5% of measured fibres were angled at -2° ≤ θ ≤ 2°. A graphical representation of results is depicted in Figure 27.

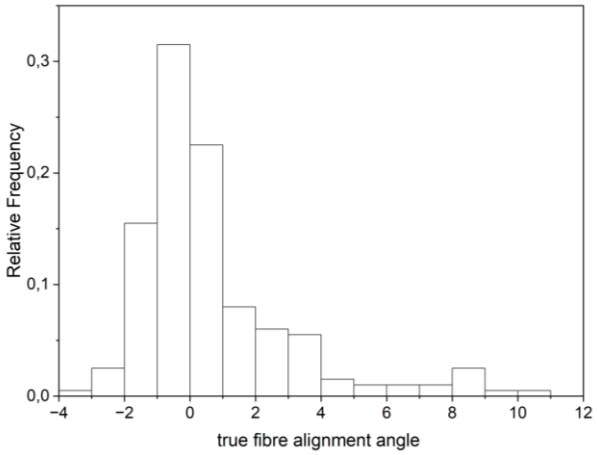

Figure 27: Fibre alignment angle distribution of CF/LDH/PEI composite laminate.

Visual inspection of sectioned laminate showed that manufacturing defects such as non uniform fibre distribution and scattered microvoids in the matrix could not be avoided entirely. Laminate sectioned at an angle of 5° is depicted in Figure 28.

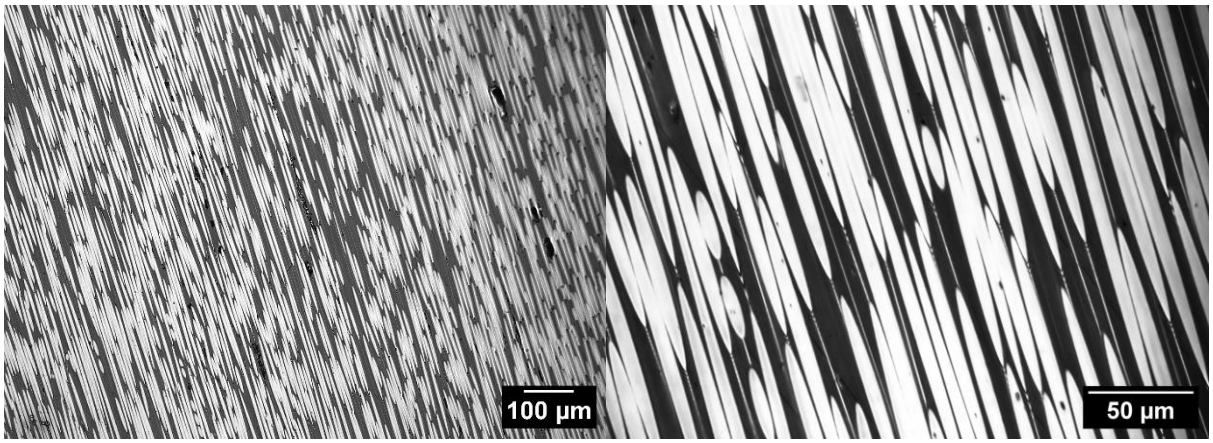

Figure 28: Optical micrographs of CF/LDH/PEI composite laminate sectioned at an angle of 5°.

Composite density was measured to be 1.56 g/cm³. With a FVF of 0.58, Equation (7) yields a void volume fraction (V_v) of 0.02. As the established threshold for V_v to minimize negative influences on material properties is greater than 0.02[47], void content does not have a significant impact on the investigated sample.

3.4.3. Interlaminar shear strength of CF/LDH/PEI laminate

The interfacial shear resistance of CF/LDH/PEI composite laminates was measured to be at τ_M (CF/LDH/PEI) > 81 ± 4.7 MPa, control was determined to be at τ_M (CF/PEI) = 74 ± 7.7 MPa. Failed CF/LDH/PEI samples displayed wedge shaped kink bands induced by fibre microbuckling. None of the specimen tested exhibited interfacial shear failure, indicating that interfacial shear resistance is higher than the results presented here. These results provide evidence that interfacial LDH deposition does not have a negative impact upon interfacial strength. Load over displacement is depicted in Figure 29 alongside the test specimens.

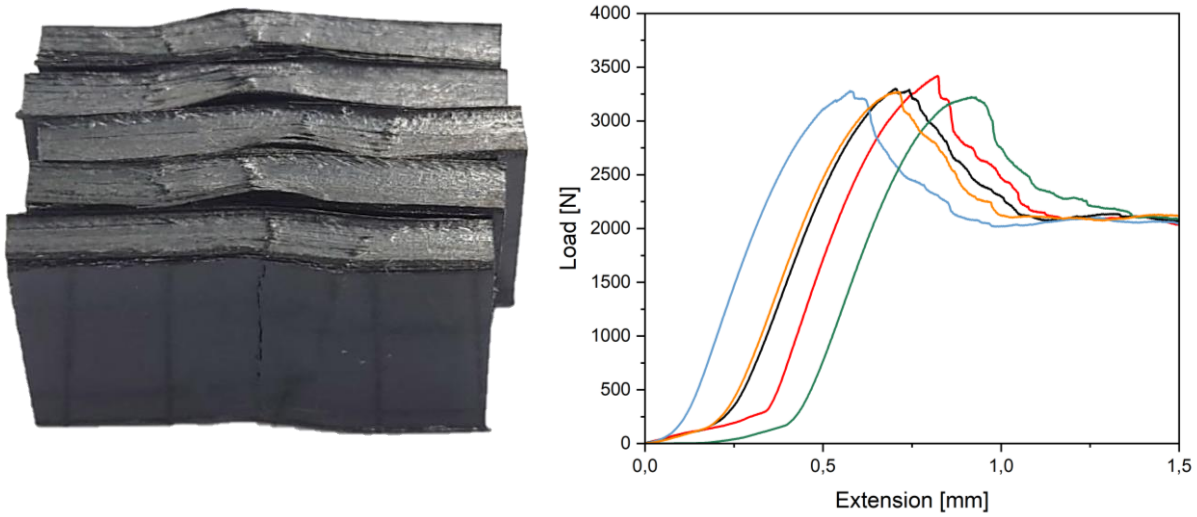

Figure 29: left: CF/LDH/PEI laminate test specimens after ILSS testing. Right: load over extension for all tested CF/LDH/PEI specimens.

4. Conclusion

Efforts made during this investigation lead to the scaled, continuous production of composite materials with an LDH interface, employing a single-step deposition process in aqueous suspension. Mechanical testing of unidirectional composite samples produced from LDH coated carbon fibres revealed interfacial shear resistance comparable to control samples, providing evidence that eventual employment of a functional nacre-mimetic interface does not come at the cost of a weaker interface. However, the objective of multilayer deposition of a LDH nanocomposite could not be met, as formation of a LDH nanocomposite though direct addition of polyanionic adsorbents comes at the cost of colloidal stability.

To achieve stable multilayer deposition of LDH with EPD, it was shown that the solvent composition must be altered. In a purely aqueous suspension, anion activity is too high, resulting in desorption of anions upon application of potential. This can be inferred from preliminary testing of EPD in 72 vol.% ethanol resulting in multilayer anodic deposition, as compared to cathodic deposition in water, alongside the negative ζ-potential of the ethanolic suspension.

Electrocoagulation experiments proved that multilayer LDH formations from an aqueous medium are possible by in-situ synthesis. Two distinct LDH structures were shown to form within the same system, independent of synthesis time and applied potential. Although further research is needed, the method appears promising, as it offers a potentially easy and cheap alternative to EPD, as well as tuneability in terms of platelet orientation, growth layer thickness and intercalant species, while also circumventing the challenge of particle and suspension engineering.

Comparative particle size analysis between SEM micrographs and DLS measurements of suspended LDH provided evidence that stable LDH suspensions still exhibit some degree of agglomeration, affecting deposition uniformity. A functional nacre mimetic interface would also likely necessitate an increased platelet aspect ratio, as strain hardening is facilitated by platelet sliding and interlocking relative to one another. Insufficient interfacial area between individual platelets will reduce the effectiveness of these mechanisms. This could potentially result in the need to revise synthesis parameters.

5. Outlook

Possible research avenues building upon insights gained in this work for both EPD and electrocoagulation are described hereafter.

5.1. Deposition of an LDH/polymer assembly

A single step electrophoretic deposition of a non-covalently assembled particle with two constituents of opposing charge can only work by inhibiting independent constituent movement. Since the direct addition of anionic polymers leads to surface charge neutralisation thereby disrupting the colloidal system, more elaborate ways of particle engineering must be performed for successful deposition.

A promising route would be the intercalation of negatively charged monomers such as sodium vinyl sulfonate (sodium 4-vinylbenzenesulfonate would likely increase interlayer thickness beyond the limits of a brick and mortar structure) either during coprecipitation or by regenerating LDO, as described by Jin et al.[48] Because the interlayer galleries of LDH force the alignment of vinyl groups, in situ polymerisation can be thermally initiated.[49] If polymerisation is selective towards interlayer galleries, suspension and therefore deposition should still be possible. The boundary condition of 90% inorganic material for nacre micromimetics can theoretically be achieved through adaption of LDH layer charge density, by adjusting M^{III}/M^{II} ratio.

5.2. Electrocoagulation

Because the anion species of the metal salt solution used for preparation of the system likely also get intercalated into LDH galleries during in situ growth, a nanocomposite can be formed by choosing an ionic compound with a polyanionic constituent, while providing the other needed metal species via the sacrificial anode. Platelet orientation appears to be dependant upon application of potential. A square wave DC function could be applied to try and selectively grow brick and mortar type structures instead of vertically aligned ones. Because the current in this system is not zero, uniform deposition is likely dependent upon resistance of individual fibres, which could pose a challenge for future applications.

6. Appendix

6.1. Measurements

6.1.1. FTIR

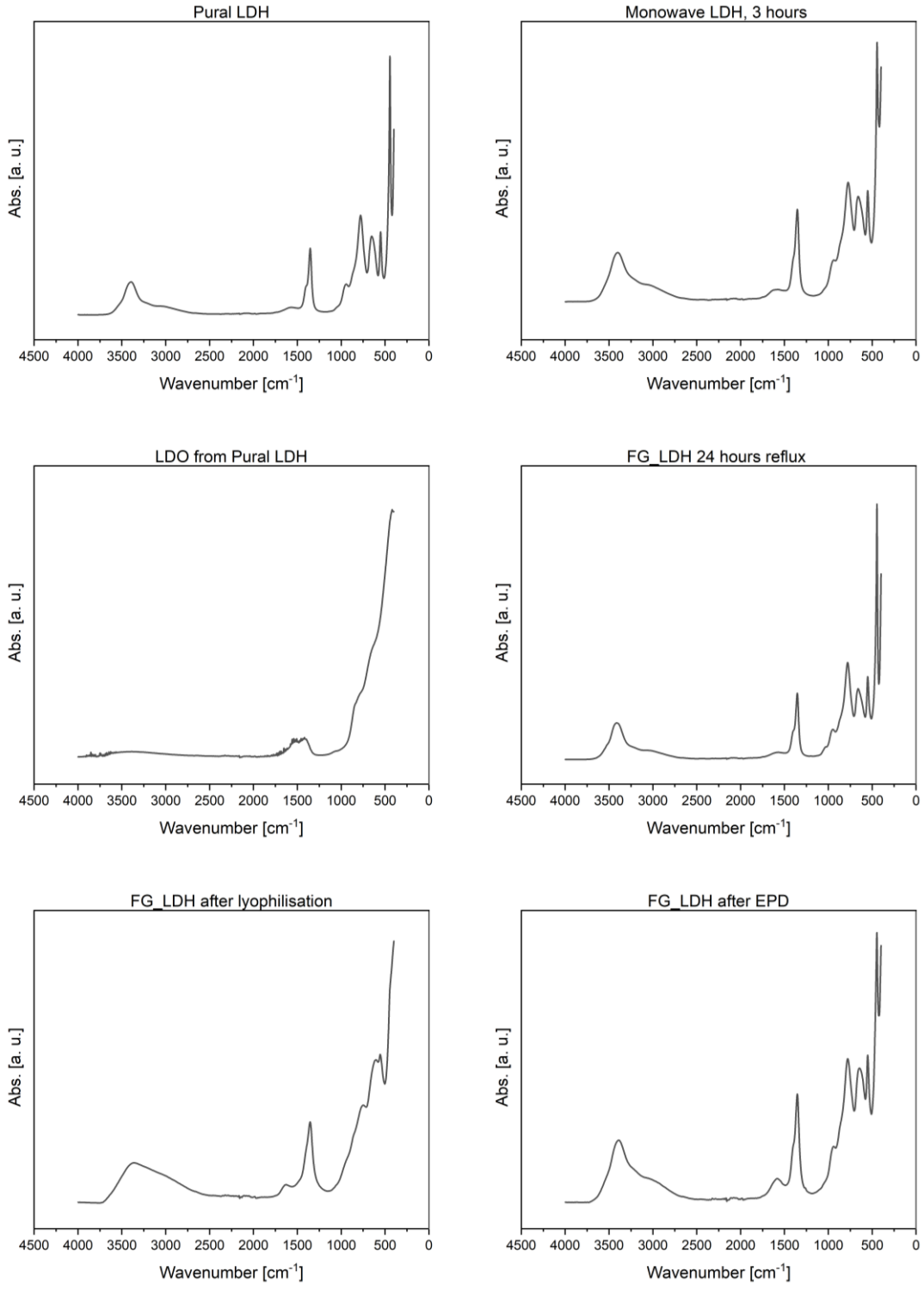

Figure 30: from left to right and top to bottom: FTIR spectra of Pural LDH, LDH peptized above ambient pressure, LDO from thermal oxidation of LDH, LDH peptized at ambient pressure, LDH after lyophilisation and after EPD

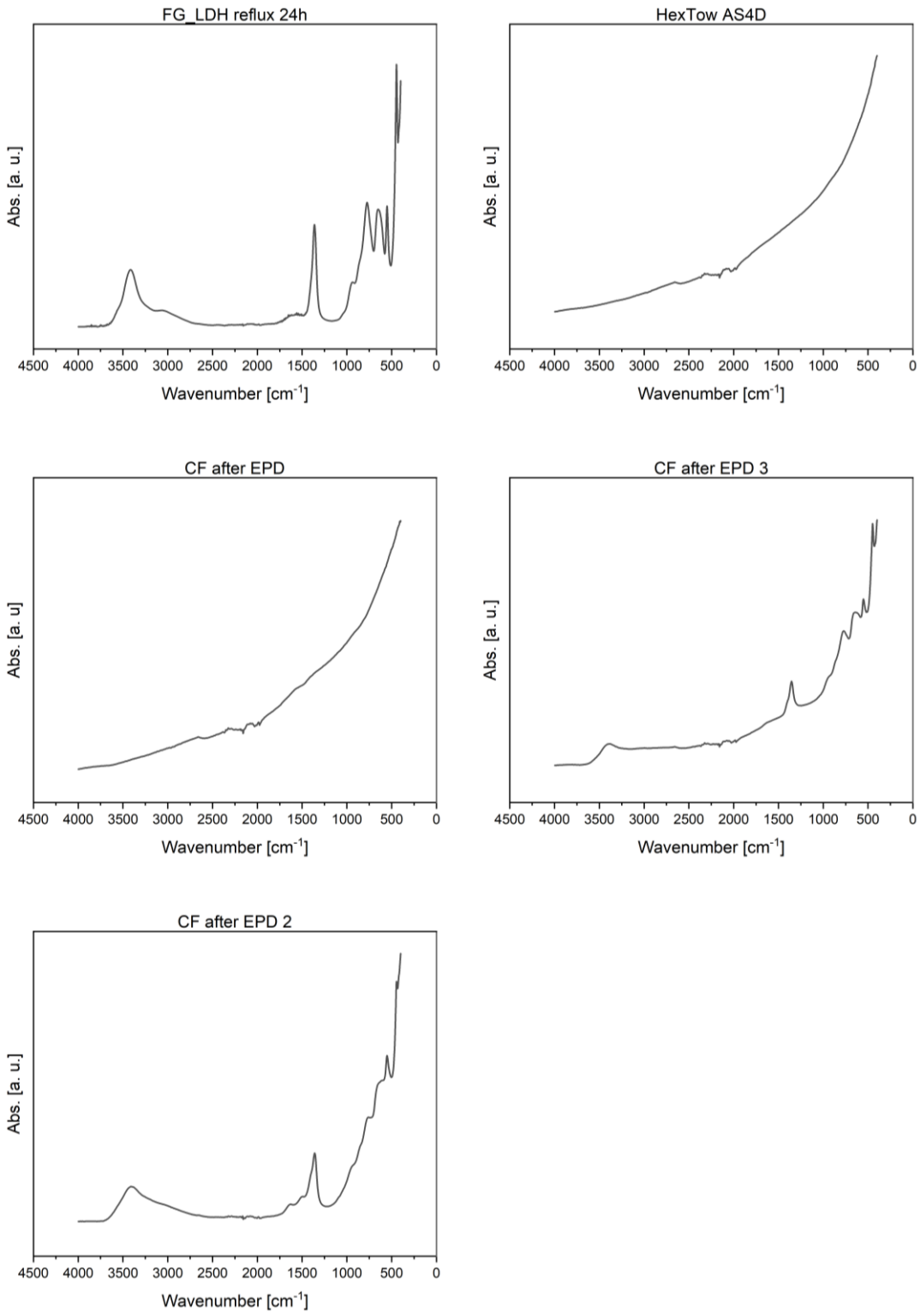

Figure 31: from left to right and top to bottom: FTIR spectra of LDH peptized at ambient pressure, pristine CF, CF after EPD

6.1.2. Short beam shear testing

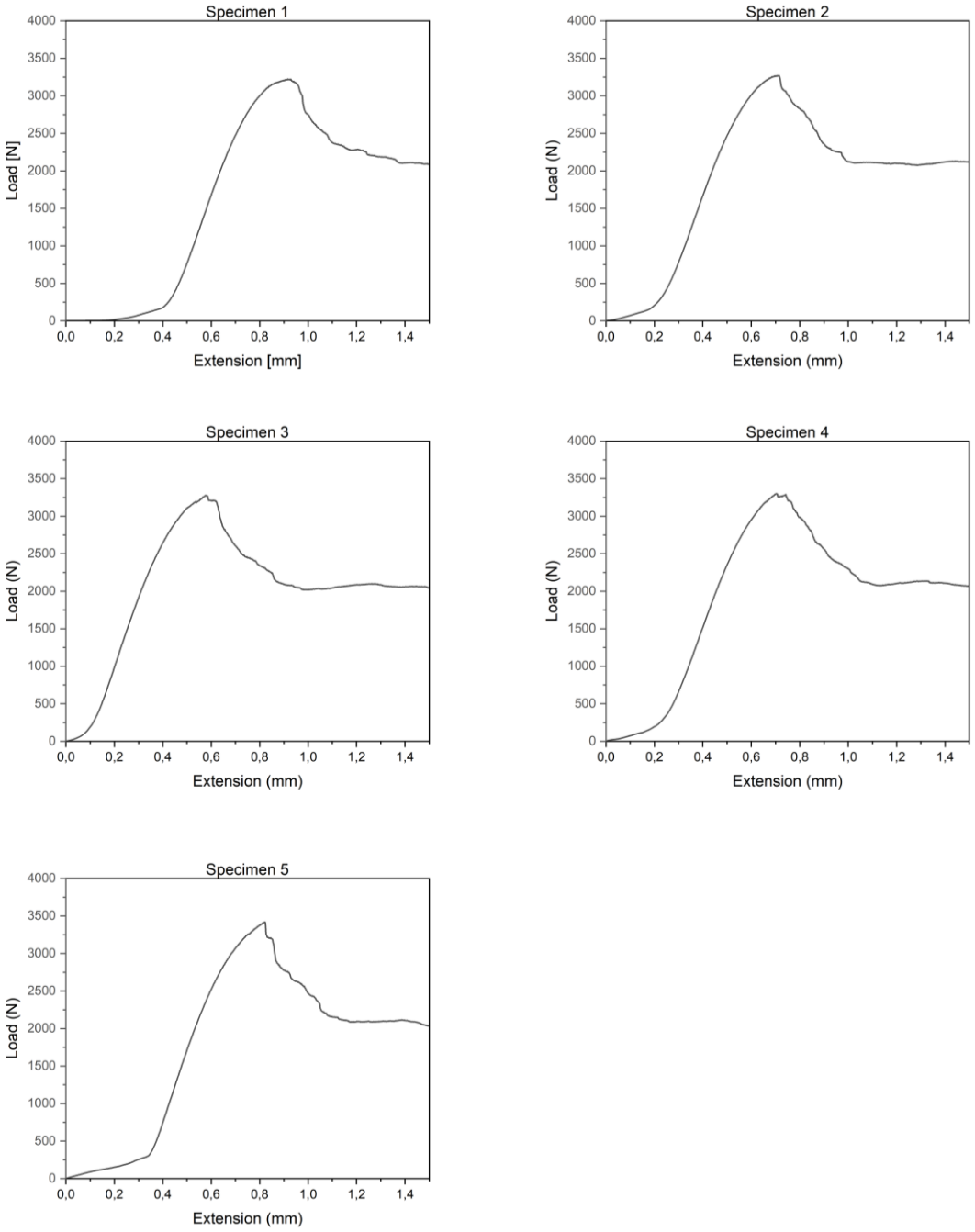

Figure 32: ILSS testing results of each individual specimen tested.

6.1.3. Sedimentation

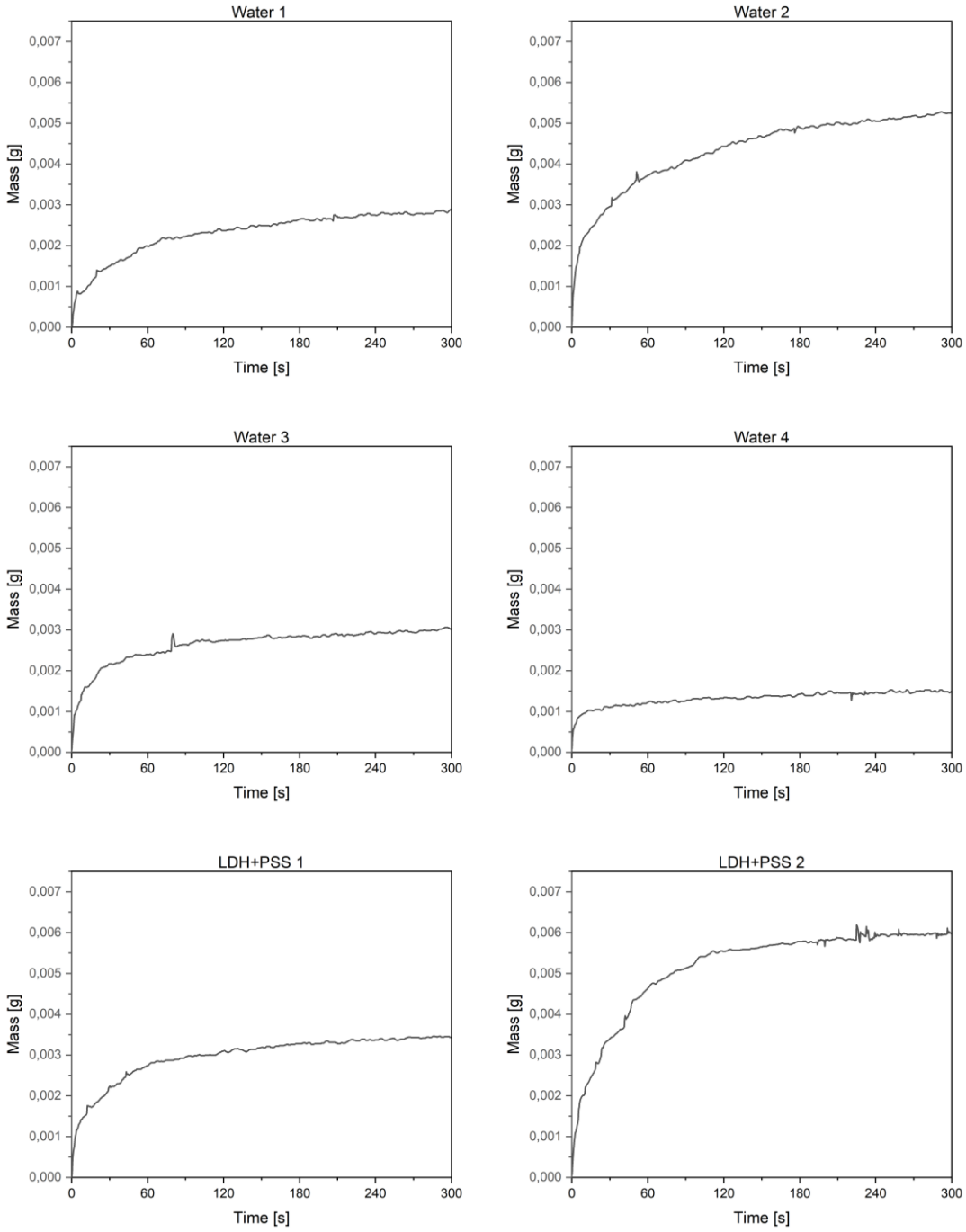

Figure 33: sedimentation as mass over time for water (graph 1 to 4) and LDH:PSS=1:9 suspensions (graph 5 and 6)

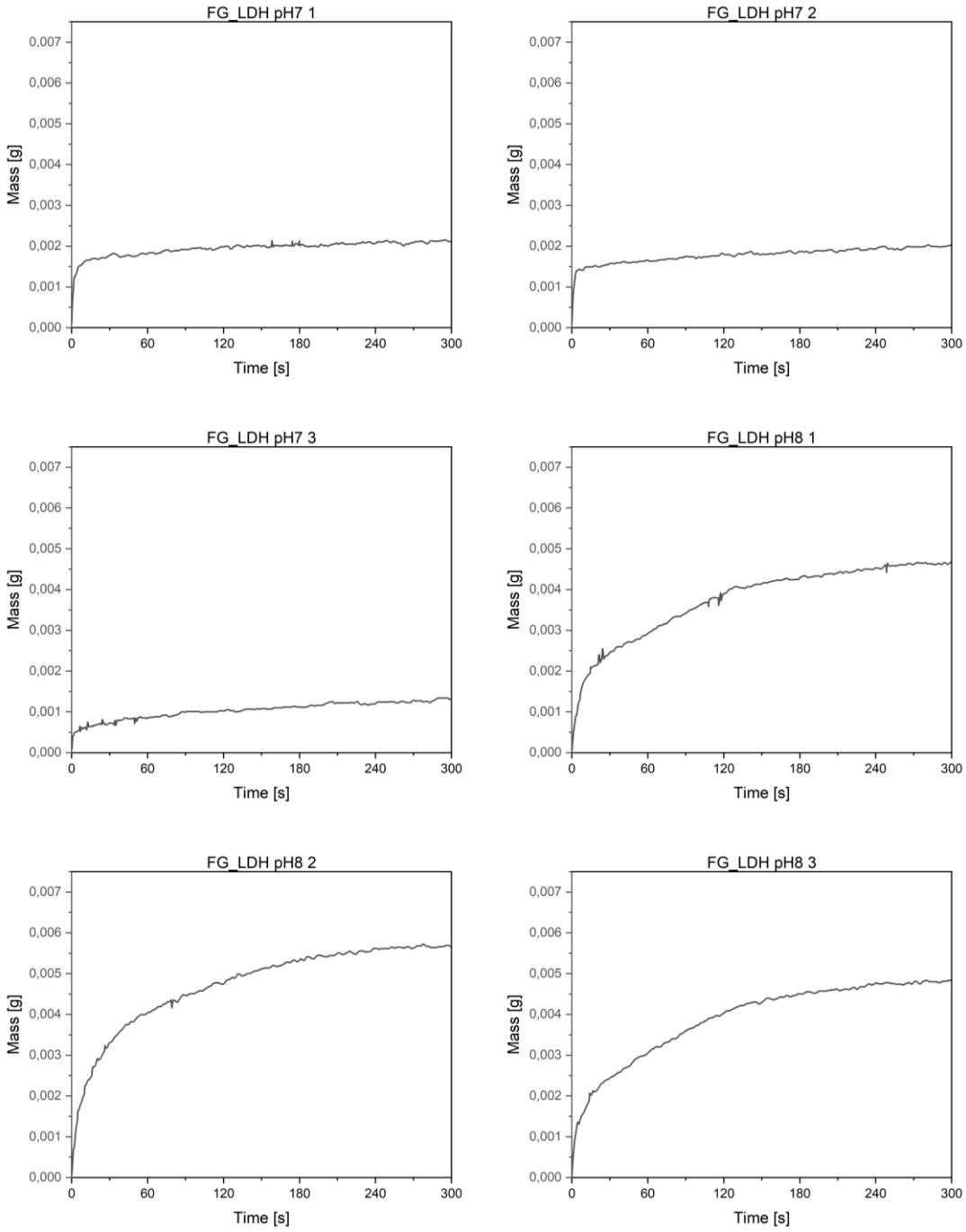

Figure 34: sedimentation as mass over time for synthesized LDH (ambient pressure) at pH 7 (graph 1 to 3) and pH 8 (graph 4 to 6)

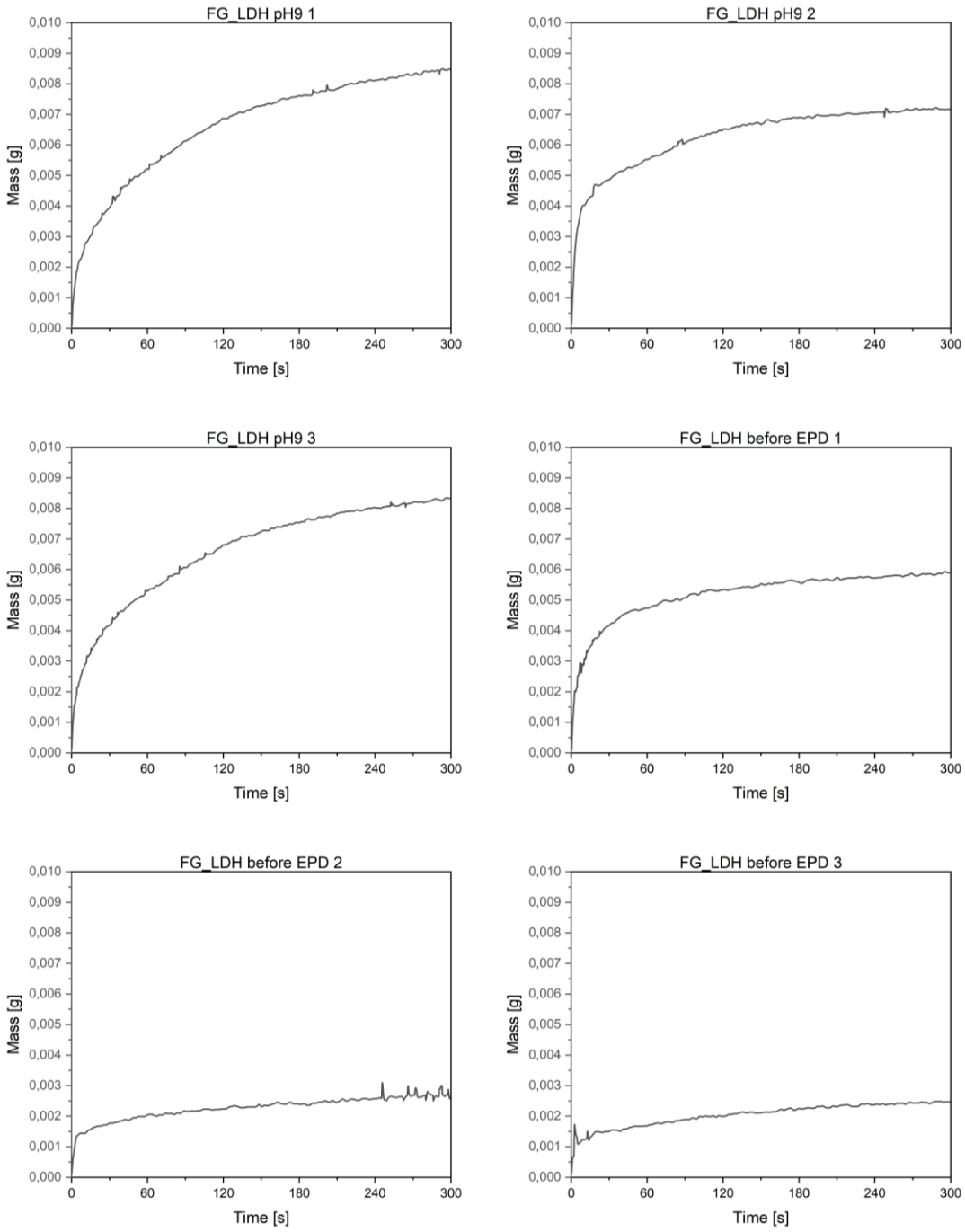

Figure 35: sedimentation as mass over time for synthesized LDH (ambient pressure) at pH 9 (graph 1 to 3) and for synthesized LDH (ambient pressure) at pH 7 before the suspension was used for EPD (graph 4 to 6)

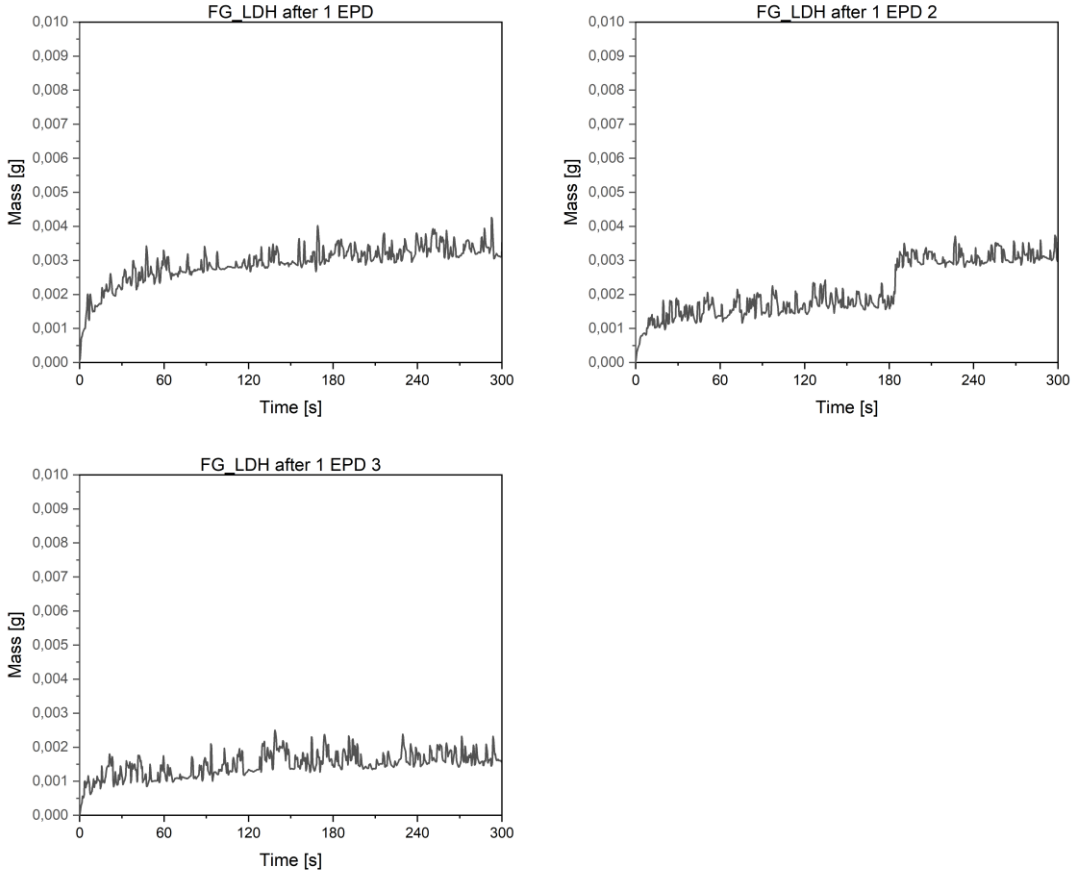

Figure 36: sedimentation as mass over time for synthesized LDH (ambient pressure) at pH 7 after the suspension was used for EPD. Random measurement error larger than other measurements because of outside influences during measurement.

6.1.4. TGA

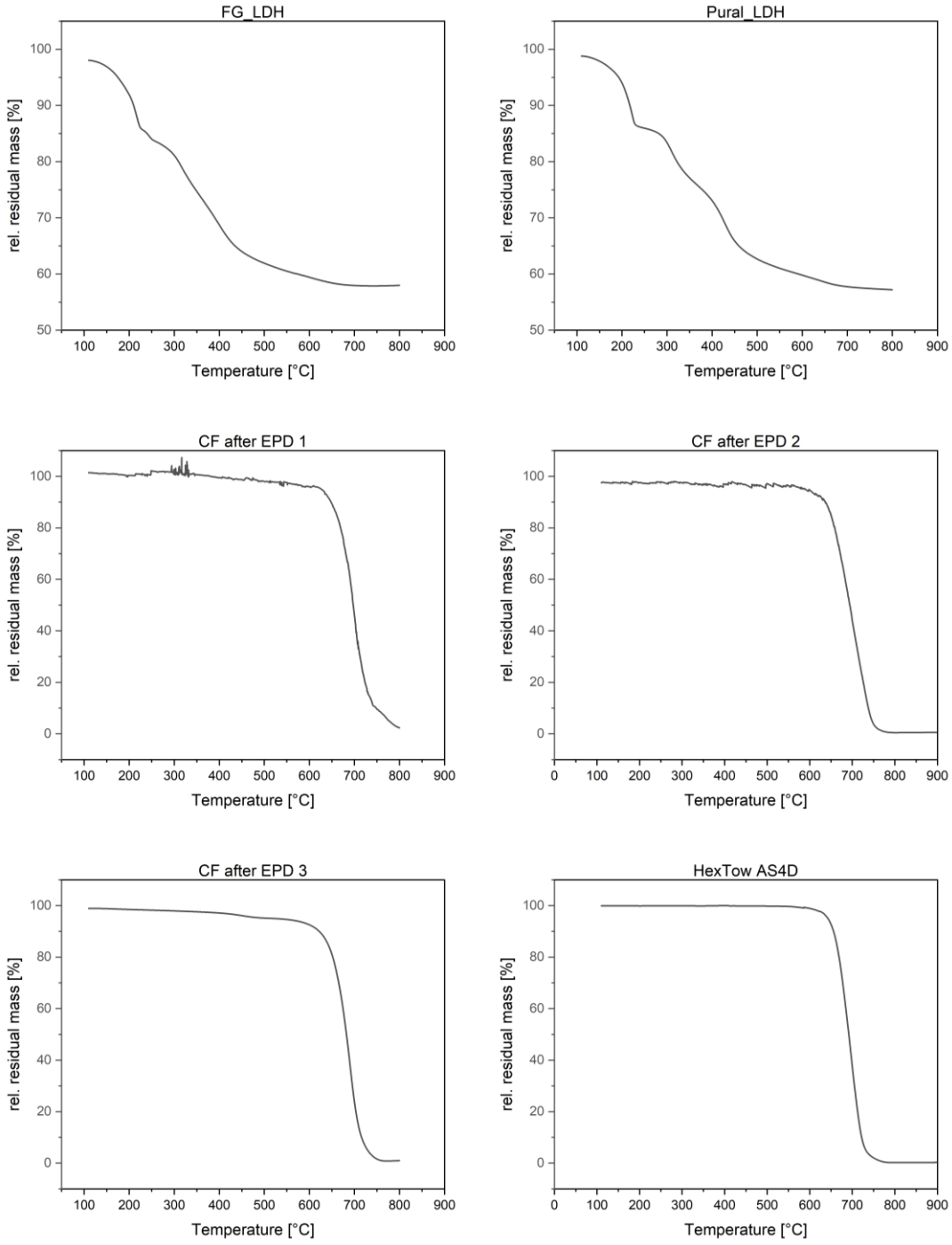

Figure 37: TGA data for synthesized and commercially obtained LDH (graph 1 and 2), for carbon fibres after LDH deposition through EPD (graph 3 to 5) and for pristine carbon fibres (graph 6). Noise in graph 3 and 4 likely from LDH decomposition and delamination from CF surface.

6.1.5. XPS

*Table 5: XPS data for pristine carbon fibres, carbon fibres dipped in LDH suspension, carbon fibres subjected to EPD at 10-30 V. Peak binding energy (peak BE); full width at half maximum (FWHM); peak area in count/second*eV (Area(P) [CPS.eV]; sensitivity factor (Q).*

CF control	Peak BE	FWHM [eV]	Area (P) [CPS.eV]	Atomic %	Q
C1s	284.69	1.4	194861.6	94.07	1
O1s	532.54	3.04	16495.77	3.3	1
N1s	401.01	2	8470.27	2.64	1

CF dipping	Peak BE	FWHM [eV]	Area (P) [CPS.eV]	Atomic %	Q
C1s	284.71	1.5	116864.53	69.66	1
O1s	532.01	2.84	82544.33	20.36	1
Mg1s	1304.41	2.13	33068.39	4.76	1
Al2p	74.34	2.35	3636.68	3.42	1
N1s	400.86	2.25	4696.08	1.81	1

EPD 10V	Peak BE	FWHM [eV]	Area (P) [CPS.eV]	Atomic %	Q
C1s	284.76	1.6	117497.51	59.11	1
O1s	532.7	2.99	133455.2	27.8	1
Mg1s	1305.1	2.56	55718.52	6.78	1
Al2p	75.26	2.51	5799.04	4.6	1
N1s	401	1.91	5262.56	1.71	1

EPD 20V	Peak BE	FWHM [eV]	Area (P) [CPS.eV]	Atomic %	Q
C1s	284.55	1.48	145717.45	62.73	1
O1s	531.84	2.48	140953.48	25.11	1
Mg1s	1304.09	1.91	60677.94	6.3	1
Al2p	74.2	2.18	6144.25	4.17	1
N1s	400.82	1.96	6102.94	1.69	1

Name	Peak BE	FWHM [eV]	Area (P) [CPS.eV]	Atomic %	Q
C1s	284.75	1.5	111701.66	53.03	1
O1s	532.01	2.48	162882.27	32	1
Mg1s	1304.26	2.04	70874.96	8.12	1
Al2p	74.4	2.14	7089.97	5.31	1
N1s	401.03	2.04	5029.54	1.54	1

6.1.6. LDH consumption during EPD: gravimetric measurement

Table 6: residual masses of dried suspension samples isolated after consecutive EPD cycles.

EPD cycle	Sample 1 [g]	Sample 2 [g]	Sample 3 [g]	Sample 4 [g]	Sample 5 [g]
0	0.00217	0.00223	0.00219	0.00223	0.00218
1	0.00217	0.00215	0.00218	0.00218	0.00218
2	0.00217	0.00210	0.00204	0.00211	0.00217
3	0.00216	0.00220	0.00214	0.00214	0.00214

6.1.7. Prepreg width and weight

Table 7: widths and masses of prepreg sections 0.2 m in length; three production runs total.

First production run		
Sample no	**Width [mm]**	**Weight [g]**
1	7	0.2274
2	7	0.2284
3	7	0.2530
4	7	0.2525
5	6.5	0.2668
6	5	0.2417
7	6	0.2352
8	5	0.2369
9	6	0.2378
10	7.5	0.2335
11	9	0.2543
12	9	0.2562
13	10	0.2737
14	10	0.2662
15	10	0.2681
16	9.5	0.2658
17	8.5	0.2642
18	8.5	0.2669
19	9	0.2719
20	9.5	0.2699
21	10	0.2630
22	10	0.2534
23	10.5	0.2512
24	10	0.2538
25	10	0.2556
26	10	0.2519
27	10	0.2539
28	10	0.2542
29	10	0.2560
30	8.5	0.2531
31	9.5	0.2515
32	9	0.2481
33	9	0.2528
34	9	0.2558
35	9	0.2510
36	9	0.2515
37	9	0.2535
38	9	0.2502
39	9	0.2515
40	9.5	0.2519
41	9	0.2539
42	9	0.2487
43	9	0.2534
44	9	0.2465
45	9	0.2518
46	9	0.2439
47	9	0.2425
48	9	0.2482
49	9	0.2482
50	8.5	0.2441
51	8.5	0.2454
52	8.5	0.2455
53	9	0.2496
54	9	0.2458
55	8.5	0.2503
56	8.5	0.2449
57	8.5	0.2481
58	8.5	0.2460
59	8	0.2542
60	8.5	0.2505
61	9	0.2502
62	9.5	0.2479
63	10	0.2481
64	8.5	0.2396
65	8	0.2488
66	8	0.2445
67	9	0.2433
68	9	0.2466
69	9	0.2502
70	9	0.2444
71	9	0.2440
72	8.5	0.2441
73	7.5	0.2507
74	7.5	0.2407
75	7.5	0.2376
76	8	0.2379
77	8	0.2474
78	8.5	0.2480
79	7.5	0.2477
80	8	0.2450
81	8	0.2451
82	8	0.2379
83	7.5	0.2503
84	7.5	0.2386
85	8	0.2506
86	8	0.2475
87	8	0.2489
88	8	0.2399
89	7	0.2515
90	7	0.2413
91	7	0.2414
92	7	0.2374

93	6.5	0.2393
94	7	0.2404
95	7	0.2444
96	8	0.2438
97	8.5	0.2421
98	9.5	0.2394
99	10	0.2469
100	10	0.2476
101	10	0.2478
102	10	0.2467
103	9	0.2461
104	9	0.2363
105	9	0.2390
106	9	0.2327
107	9	0.2421
108	9	0.2372
109	9	0.2408
110	9	0.2370
111	9	0.2421
112	9	0.2383
113	9	0.2377
114	8.5	0.2357
115	8	0.2440

Second production run		
Sample no	**Width [mm]**	**Weight [g]**
1	10	0.235
2	9.5	0.231
3	8.5	0.229
4	8	0.219
5	8	0.219
6	8	0.218
7	9	0.225
8	9.5	0.231
9	10	0.239
10	9.5	0.250
11	9.5	0.244
12	9	0.233
13	9	0.226
14	8.5	0.223
15	8.5	0.219
16	9	0.222
17	9	0.222
18	8.5	0.221
19	8.5	0.220
20	9	0.220
21	9	0.223
22	9	0.225
23	9	0.229
24	8.5	0.227
25	9	0.227
26	9	0.225
27	9	0.224
28	9	0.223
29	9	0.218
30	9	0.219
31	9	0.220
32	9	0.225
33	9	0.224
34	8.5	0.222
35	8.5	0.225
36	8.5	0.226
37	8.5	0.220
38	8.5	0.219
39	8.5	0.219
40	8.5	0.220
41	8.5	0.219
42	8.5	0.226
43	8.5	0.227
44	8.5	0.222
45	8	0.217
46	8	0.216
47	8.5	0.220
48	8.5	0.218
49	9	0.224
50	9	0.227
51	9	0.227
52	8.5	0.225
53	8	0.218
54	8	0.219
55	8	0.220
56	8.5	0.223
57	8	0.221
58	8	0.224
59	8	0.220
60	8	0.225
61	8	0.222
62	8	0.222
63	8	0.215
64	8	0.219
65	8	0.217
66	7.5	0.213
67	7	0.208
68	7.5	0.217
69	8	0.219
70	7.5	0.216
71	7	0.219
72	7.5	0.220
73	8	0.224
74	8	0.222
75	8	0.225
76	8	0.229
77	7.5	0.227
78	8	0.226
79	8	0.229

80	8	0.222
81	7.5	0.221
82	7.5	0.221
83	7.5	0.219
84	8	0.221
85	8	0.220
86	7	0.218
87	7	0.216
88	7.5	0.221
89	8	0.220
90	8	0.221
91	8	0.220
92	8	0.223
93	7.5	0.227
94	7.5	0.225
95	7.5	0.228
96	7	0.225
97	7	0.231
98	7.5	0.228
99	8	0.228
100	7.5	0.225
101	7.5	0.225
102	8	0.227
103	8	0.222
104	8	0.224
105	7	0.222
106	7	0.218
107	7	0.220
108	7.5	0.224
109	7	0.219
110	7	0.212
111	7	0.214
112	7.5	0.217
113	7	0.221
114	6.5	0.225
115	6	0.255
116	6	0.267
117	7	0.269
118	7.5	0.267
119	7	0.272
120	8	0.268
121	9	0.275
122	8.5	0.275
123	8.5	0.273
124	9	0.270
125	9	0.265
126	5	0.229
127	5	0.213
128	5	0.212
129	5	0.216
130	6	0.218
131	7.5	0.233
132	9.5	0.243
133	9	0.248
134	8	0.250
135	7.5	0.250

Third production run		
Sample no	**Width [mm]**	**Weight [g]**
1	7.5	0.312
2	7	0.318
3	8	0.354
4	8	0.384
5	9	0.353
6	9	0.377
7	12	0.506
8	10	0.285
9	10	0.286
10	9	0.251
11	10	0.338
12	10	0.341
13	10	0.338
14	10	0.350
15	10	0.340
16	10	0.342
17	10	0.325
18	10	0.319
19	10	0.310
20	9.5	0.306
21	9.5	0.321
22	9	0.350
23	9.5	0.375
24	9.5	0.362
25	9.5	0.358
26	9.5	0.385
27	9.5	0.388
28	9.5	0.394
29	9.5	0.409
30	9.5	0.413
31	9.5	0.381
32	9.5	0.362
33	9.5	0.372
34	9.5	0.375
35	9.5	0.364
36	9.5	0.369
37	9.5	0.361
38	10	0.352
39	10	0.344
40	10	0.361
41	10	0.355
42	9	0.357
43	8.5	0.324
44	9	0.323
45	9	0.315
46	9.5	0.339

47	9.5	0.333
48	9	0.313
49	9	0.311
50	9	0.309
51	8	0.300
52	8	0.308
53	9	0.309
54	9	0.320
55	7	0.312
56	7.5	0.319
57	8.5	0.320
58	9	0.312
59	8	0.300
60	9.5	0.316
61	10.5	0.313
62	10.5	0.309
63	10.5	0.307
64	10.5	0.302
65	10.5	0.303
66	10.5	0.305
67	10.5	0.306
68	10.5	0.303
69	10	0.291
70	10	0.290
71	10	0.301
72	9	0.301
73	10	0.303
74	10	0.295
75	10	0.297
76	9.5	0.299
77	9.5	0.288
78	9.5	0.281
79	9.5	0.275
80	9	0.285
81	9	0.285
82	9	0.289
83	9.5	0.295
84	10	0.307
85	10	0.299
86	10	0.289
87	10	0.298
88	10	0.290
89	10	0.281
90	10	0.277
91	10	0.271
92	9	0.267
93	9	0.269
94	8.5	0.265
95	8	0.272
96	8.5	0.263
97	8	0.265
98	8	0.272
99	8	0.266
100	8	0.266
101	8.5	0.271
102	8.5	0.260
103	8.5	0.265
104	9	0.268
105	9	0.264
106	8	0.261
107	8	0.262
108	8	0.267
109	8	0.278
110	8	0.268
111	7.5	0.258
112	7.5	0.252
113	8	0.256
114	8.5	0.259
115	8.5	0.254
116	8.5	0.260

6.1.8. Fibre alignment data

Table 8: minor and major axes of fibres cross sectioned at an angle of five degrees. Measurement was performed using imageJ software

Sample no	Major axis [µm]	Minor axis [µm]
1	35.7	2.48
2	23.6	2.8
3	44.6	3.23
4	57.1	3.18
5	48.8	3.21
6	26.3	3.4
7	63.7	3.8
8	29.5	3.5
9	23.7	2.93
10	49.5	3.59
11	38.5	3.57
12	20.6	3.64
13	53.9	3.94
14	39.2	3.52
15	16.4	3.37
16	65	3.06
17	53.8	3.33
18	48.1	3.54
19	46.2	3.11
20	18.1	3.8
21	45.1	3.48
22	79.2	3.24
23	42.7	3.53
24	51.6	3.27
25	53.3	3.44
26	56.2	3.32
27	14.3	3
28	28.1	3.5
29	43.2	3.53
30	26.2	3.11
31	56	3.47
32	35.6	3.24
33	47.8	3.47
34	48.9	3.27
35	50.1	3.12
36	50	3.16
37	57.1	3.43
38	41.3	3.01
39	60.9	3.12
40	40.3	3.36
41	53	3.58
42	101.8	3.47
43	49.7	2.92
44	71.8	3.17
45	48.7	3.17
46	68.2	3.1
47	55.5	3.42
48	29	3.01
49	49.6	3.37
50	23	3.63
51	16.8	3.08
52	53.1	3.53
53	55	3.52
54	36.7	3.75
55	56.2	3.55
56	58.4	3.32
57	40.8	3.44
58	46.2	3.3
59	51.6	3.25
60	49	3.44
61	36.8	3.16
62	45.2	3.36
63	29.9	3.77
64	55.9	3.42
65	50.3	3.24
66	48.7	3.12
67	73.3	3.72
68	61.6	3.48
69	49.8	3.62
70	37.8	3.31
71	65.7	3.9
72	34.4	3.34
73	34.7	3.38
74	48	3.47
75	40.5	3.38
76	37.8	3.3
77	46.3	2.96
78	19.8	3.17

79	27.5	3.64
80	20.3	3.01
81	52.4	3.21
82	33.6	3.75
83	42.5	3.42
84	41.1	3.12
85	14.1	3.12
86	27.3	3.01
87	36.4	3.06
88	40.9	3.06
89	67.1	2.76
90	38.3	3.47
91	45.4	3.27
92	48.1	3.46
93	15.6	3.42
94	52.2	3.12
95	14.8	3.42
96	39.2	3.2
97	51.8	3.7
98	14.9	3.18
99	54.8	2.86
100	49.6	3.37
101	89.7	1.75
102	40.2	2.43
103	28.4	2.62
104	49.9	2.22
105	33.7	2.19
106	39.7	2.22
107	33.1	2.43
108	52	2.65
109	32.8	2.22
110	36.6	2.69
111	34.7	2.43
112	46.5	3.07
113	74.4	2.69
114	67.6	2.69
115	168	2.86
116	161	2.96
117	48.4	2.43
118	26.4	3.07
119	41.6	2.96
120	13.1	3.29
121	28.7	2.42
122	16.6	2.59
123	46.4	3
124	42.6	3.03
125	40.9	2.72
126	45.7	2.86
127	22.5	2.22
128	29.4	2.46
129	63.4	2.76
130	51.4	2.48
131	73	2.62
132	22.7	2.93
133	51.6	2.5
134	48.7	2.76
135	127	2.62
136	48.1	2.89
137	68.1	2.51
138	22.5	2.52
139	31.8	2.21
140	61.8	2.45
141	138	5.5
142	73.7	5.91
143	60.7	4.54
144	111	5.65
145	117	5.5
146	117	5.91
147	86.5	5.65
148	87.3	5.5
149	37.1	4.96
150	82.2	5.5
151	46.7	5.25
152	104	5.5
153	50.2	5.65
154	82.1	5.83
155	47.3	5.5
156	43.4	6.06
157	115	6.23
158	67.7	6.06
159	57.2	5.44
160	70.7	5.09
161	35.6	2.52
162	43.6	2.7
163	18.8	2.72
164	29.5	2.56
165	26.5	2.82
166	25.4	2.36
167	39.7	2.77
168	62.1	2.42
169	32.5	2.46
170	49.4	2.86
171	21.3	2.69
172	59	2.79
173	27.8	2.72
174	81	2.14

175	40.3	2.28
176	52.2	2.9
177	41.2	2.66
178	21.8	2.7
179	38.8	3.06
180	44.2	2.97
181	59.3	3.91
182	35.7	3.5
183	40.8	3.15
184	105	4
185	66.8	3.54
186	66.8	3.74
187	38.8	3.66
188	16.2	3.15
189	86.9	3.4
190	62.6	3.5
191	102	4.1
192	28.7	3.4
193	45.2	3.59
194	58.9	3.33
195	63.1	3.66
196	96.8	3.66
197	56.4	3.27
198	33.2	4.34
199	38	3.15
200	47.3	4

6.1.9. SEM particle size distribution data (from suspension)

Table 9: area of LDH particles isolated from suspension. Analysis of SEM micrographs using imageJ software.

Sample no	Area [nm²]
1	1725
2	4236
3	7964
4	5875
5	5388
6	2307
7	2285
8	1571
9	2027
10	1805
11	2187
12	1628
13	9655
14	2425
15	5570
16	2833
17	3931
18	10225
19	1684
20	947
21	1423
22	1591
23	529
24	926
25	4510
26	2382
27	2055
28	4981
29	3377
30	1460
31	5349
32	10573
33	1290
34	3342
35	1126
36	991
37	4478
38	5166
39	2464
40	1360
41	3811
42	2251
43	2805
44	7694
45	1119
46	1913
47	2911
48	1762
49	1917
50	3855
51	4853
52	4880
53	2522
54	7304
55	2699
56	2309
57	6928
58	777
59	1932
60	2087
61	1775
62	3363
63	4784
64	372
65	1621
66	980
67	2913
68	2101
69	3789
70	3466

71	1565
72	4578
73	10575
74	726
75	3965
76	4205
77	2943
78	5601
79	6288
80	1810
81	757
82	1275
83	8119
84	4705
85	1398
86	1265
87	1471
88	4205
89	1915
90	1414
91	1725
92	1879
93	6361
94	4326
95	813
96	4305
97	5343
98	1464
99	2918
100	4422
101	3447
102	3966
103	5851
104	3878
105	5102
106	3734
107	8074
108	844
109	1683
110	944
111	2852
112	3512
113	2746
114	2005
115	2578
116	4004
117	3947
118	1590

119	3031
120	12791
121	1924
122	1269
123	1589
124	649
125	797
126	1108
127	4161
128	2179
129	1363
130	4555
131	3395
132	2976
133	6193
134	3069
135	6734
136	2884
137	1486
138	2064
139	6426
140	1743
141	3115
142	5108
143	10632
144	1627
145	4226
146	3096
147	2098
148	2155
149	6472
150	3243
151	1852
152	5880
153	3655
154	2426
155	1804
156	2919
157	2884
158	1187
159	1548
160	1936
161	1117
162	3310
163	3711
164	3691
165	2459
166	4622

167	3293
168	1642
169	1915
170	1499
171	3420
172	3538
173	1499
174	1536
175	2916
176	2542
177	9552
178	7093
179	2987
180	1187
181	2843
182	6884
183	822
184	3305
185	2384
186	1913
187	13963
188	1885
189	4027
190	966
191	2056
192	986
193	2818
194	4809
195	4722
196	2053
197	4881
198	2203
199	2658
200	2222
201	2063
202	750
203	5404
204	1120
205	2115
206	8152
207	1919
208	4114
209	939
210	2626
211	3356
212	5400
213	1707
214	3346

215	5293
216	2574
217	1254
218	2443
219	3358
220	1863
221	2341
222	1124
223	5187
224	2873
225	1903
226	2822
227	10913
228	2363
229	936
230	11739
231	2919
232	3411
233	2521
234	1524
235	1471
236	2638
237	723
238	4248
239	1663
240	1603
241	1543
242	1580
243	1626
244	1617
245	2832
246	7991
247	1369
248	2938
249	1540
250	1827
251	1360
252	4369
253	791
254	5417
255	6405
256	3156
257	1111
258	3202
259	2579
260	2958
261	2903
262	1417

263	4587
264	2274
265	3038
266	1467
267	4179
268	2323
269	2361
270	3900
271	8769
272	3873
273	2267
274	3645
275	4471
276	1030
277	1304
278	1003
279	3479
280	1606
281	1113
282	1721
283	1072
284	2735
285	1204
286	1619
287	6704
288	1185
289	2335
290	3041
291	2594
292	2082
293	3108
294	1864
295	2870
296	6015
297	7178
298	5770
299	1352
300	2083
301	1187
302	3649
303	2109
304	1441
305	1357
306	2320
307	2761
308	1540
309	686
310	3120

311	9556
312	1126
313	3279
314	348
315	2622
316	3488
317	4302
318	2450
319	1899
320	2285
321	1768
322	703
323	5680
324	4845
325	2579
326	4071
327	3497
328	3753
329	2649
330	3140
331	1259
332	1251
333	2980
334	1938
335	1543
336	7544
337	1557
338	9994
339	4714
340	3403
341	2724
342	832
343	2991
344	2779
345	2941
346	1327
347	1961
348	15263
349	1731
350	2419
351	911
352	7553
353	8062
354	461
355	7122
356	740
357	3009
358	708

359	2158
360	3785
361	2724
362	10649
363	1912
364	7391
365	4372
366	2341
367	4102
368	3040
369	4274
370	1015
371	966
372	3922
373	5467
374	4151
375	412
376	1250
377	4093
378	3769
379	2933
380	5805
381	724
382	2520
383	1808
384	7212
385	1227
386	16617
387	2014
388	3287
389	1927
390	6112
391	4352
392	1321
393	3303
394	1314
395	2874
396	3950
397	4873
398	1794
399	3410
400	4623
401	4973
402	4171
403	3609
404	2383
405	1955
406	5275

407	1175
408	725
409	4370
410	4766
411	1626
412	901
413	2266
414	1081
415	1390
416	4525
417	2301
418	4926
419	2276
420	3435
421	1728
422	792
423	3675
424	3295
425	7341
426	5098
427	2832
428	2731
429	2667
430	5643
431	3603
432	2390
433	2470
434	2154
435	5454
436	1476
437	2860
438	1749
439	6092
440	1626
441	2014
442	883
443	7303
444	7364
445	7420
446	2724
447	3307
448	5432
449	2507
450	1843
451	6997
452	3513
453	948
454	1118

455	2093
456	8811
457	6508
458	3571
459	2821
460	6391
461	2419
462	1556
463	3595
464	2213
465	5295

6.1.10. SEM particle size distribution data (from fibre)

Table 10: area of LDH particles deposited on CF surface by means of EPD. Analysis of SEM micrographs using imageJ software.

Sample no	Area [nm²]
1	9813
2	5739
3	12396
4	1908
5	5968
6	5925
7	13716
8	3874
9	10947
10	1851
11	1923
12	1707
13	2626
14	1865
15	3788
16	1679
17	8508
18	7001
19	2869
20	3630
21	3745
22	10545
23	6428
24	2367
25	11879
26	12052
27	6055
28	8436
29	3042
30	5136
31	3085
32	10560
33	6801
34	7389
35	1306
36	1822
37	1923
38	3587
39	1894
40	2970
41	7948
42	2166
43	1865
44	3773
45	6040
46	1621
47	10617
48	2654
49	2539
50	6356
51	1119
52	2253
53	6011
54	1492
55	4849
56	2869
57	6227
58	3372
59	6198
60	2037
61	7288
62	8207
63	3300
64	2783
65	4864
66	2123
67	7905
68	4161
69	6958
70	1750
71	7288
72	4347
73	12238
74	9383
75	16155
76	3989
77	2425
78	1492
79	4907
80	4448
81	5308
82	1994
83	4347
84	2999
85	3070
86	3745
87	5796
88	4792
89	1937
90	6040
91	2855
92	3257
93	3343
94	1650
95	3472
96	2095
97	5725
98	1664
99	1765
100	6169
101	1506
102	11205
103	3415
104	2740
105	3859
106	2669
107	5265
108	3630
109	1937
110	1607
111	1951
112	2927
113	4763
114	1808
115	2138
116	3960
117	8092
118	8106
119	9842
120	6600
121	9799
122	5380
123	5194
124	6772

125	3458
126	1478
127	3888
128	3572
129	3730
130	11205
131	2683
132	7418
133	1879
134	2281
135	4935
136	4605
137	2539
138	3486
139	4864
140	2425
141	1650
142	3544
143	6270
144	9555
145	3458
146	2525
147	2310
148	1291
149	6126
150	3673
151	5280
152	6915
153	1822
154	12066
155	5151
156	4735
157	10459
158	3673
159	3257
160	5811
161	2009
162	2826
163	3099
164	2740
165	1420
166	2281
167	2568
168	3472
169	4778
170	13228
171	7719
172	10143

173	5294
174	3644
175	3644
176	3042
177	8422
178	2999
179	4304
180	5194
181	2037
182	2324
183	5265
184	5395
185	10545
186	6069
187	7403
188	7905
189	6442
190	7633
191	4864
192	4505
193	4433
194	7676
195	4448
196	3171
197	2783
198	8953
199	3415
200	9512
201	4849
202	4634
203	1736
204	5825
205	2511
206	2052
207	4907
208	3816
209	5868
210	4362
211	8034
212	3314
213	3486
214	12726
215	2152
216	7073
217	4089
218	6112
219	3429
220	3085

221	2166
222	4275
223	1980
224	12726
225	1492
226	7188
227	2482
228	13429
229	2080
230	7547
231	3845
232	5854
233	1779
234	1808
235	3142
236	3271
237	6801
238	4060
239	2453
240	3615
241	3859
242	5868
243	4634
244	2970
245	2712
246	3788
247	3788
248	3156
249	15151
250	2956
251	2554
252	6600
253	1750
254	2898
255	6471
256	5911
257	2611
258	10760
259	5308
260	2669
261	4362
262	3429
263	2740
264	3529
265	4534
266	3716
267	5753
268	5495

269	1650
270	1736
271	11191
272	7360
273	3874
274	5265
275	4519
276	2396
277	2152
278	3702
279	1793
280	2095
281	1765
282	7561
283	2812
284	2496
285	5481
286	2740
287	2669
288	3831
289	3501
290	3759
291	8336
292	2496
293	3314
294	6370
295	5208
296	2568
297	3601
298	4046
299	3242
300	2912
301	4118
302	5438
303	5638
304	15079
305	7073
306	3687
307	4132
308	6714
309	4806
310	2568
311	6442
312	2626
313	2869
314	10201
315	4089
316	4821

317	2597
318	6628
319	8580
320	4892
321	1607
322	5337
323	9900
324	8121
325	2195
326	14692
327	4620
328	3802
329	6743
330	5251
331	3415
332	3745
333	4620
334	3042
335	5897
336	4706
337	11205
338	4103
339	3156
340	2209
341	3372
342	2224
343	5868
344	3056
345	10172
346	9641
347	4806
348	6026
349	6112
350	6600
351	9254
352	5796

6.1.11. DLS and Zeta potential

Table 11: DLS and zeta potential measurements performed throughout this work.

Sample name	Avg. particle diameter [nm]			Zeta potential [mV]		
FG_LDH 001	196.8	185.6	204.0	28.4	28.6	29.0
FG_LDH 001_PSS	--	--	--	-18.6	-18.7	-18.9
FG_LDH 004	155.9	155.4	157.2	28.7	28.9	29.3
FG_LDH 006 72h	>1000	>1000	>1000	-19.2	-18.8	-18.5
FG_LDH 009 4h pH7	820.5	823.3	595.4	25.5	25.3	26.2
FG_LDH 009 3h pH7	173.9	169.8	169.2	27.9	27.7	28.5
FG_LDH 009 2h pH7	151.5	149.3	148.4	25.3	26.5	26.6
FG_LDH 009 4h pH8	--	--	--	12.7	12.9	13.0
FG_LDH 009 3h pH8	--	--	--	12.2	13.2	12.9
FG_LDH 009 2h pH8	--	--	--	14.2	15.9	15.5
FG_LDH 009 4h pH9	--	--	--	8.86	8.98	8.68
FG_LDH 009 3h pH9	--	--	--	10.1	10.7	10.7
FG_LDH 009 2h pH9	--	--	--	11.4	12.2	12.2
FG_LDH 010 4h pH7	123.4	124.9	122.5	28.1	29.1	28.2
FG_LDH 010 3h pH7	143.7	140.9	138.2	27.3	28.2	28.4
FG_LDH 010 2h pH7	189.9	185.8	183.8	27.5	27.8	26.5
FG_LDH 010 1h pH7	270.3	267.0	264.9	28.4	27.2	27.3
FG_LDH 010 4h pH8	590.5	629.8	683.0	11.4	12.3	12.1
FG_LDH 010 3h pH8	263.4	268.1	276.0	13.0	12.4	12.6
FG_LDH 010 2h pH8	318.0	319.4	325.7	12.3	12.7	12.6
FG_LDH 010 1h pH8	434.9	419.0	405.6	13.4	13.4	14.0
FG_LDH 010 4h pH9	>1000	>1000	>1000	10.7	10.4	10.1
FG_LDH 010 3h pH9	>1000	>1000	>1000	9.94	10.2	9.82
FG_LDH 010 2h pH9	>1000	>1000	>1000	9.16	8.97	9.64
FG_LDH 010 1h pH9	>1000	>1000	>1000	10.7	9.66	10.3
FG_LDH 010 4h pH10	>1000	>1000	>1000	8.47	9.25	8.59
FG_LDH 010 3h pH10	>1000	>1000	>1000	8.24	9.74	9.71
FG_LDH 010 2h pH10	>1000	>1000	>1000	8.85	9.43	8.16
FG_LDH 010 1h pH10	>1000	>1000	>1000	10.6	10.9	10.4
FG_LDH 012 10min 0.1wt%	157.0	155.1	153.9	21.5	21.1	22.0
FG_LDH 012 10min 0.2wt%	99.34	97.19	96.61	27.1	27.4	27.2
FG_LDH 012 2h 0.2wt%	63.32	62.61	62.34	29.2	28.3	31.0
FG_LDH 013	48.97	51.07	50.22	34.1	34.4	34.0
FG_EPD 0.1wt%	52.22	51.07	51.46	31.6	33.1	30.8
FG_LDH 24.5. batch 1	128.2	125.6	125.4	29.9	29.5	29.6
FG_EPD 28.5.	55.40	55.15	55.01	30.8	30.0	29.4
FG_EPD 28.5. 1 cycle	173.1	180.7	170.9	32.0	33.7	30.8
FG_EPD sed exp 3.6.	68.49	67.36	67.60	25.9	25.2	26.6
FG_EPD sed exp 3.6. 1 epd	111.4	114.3	113.7	32.9	33.4	33.5
FG_EPD sed exp 3.6. 2 epd	155.2	161.5	159.5	35.0	34.5	32.9
FG_EPD sed exp 3.6. 3 epd	190.6	202.7	194.3	34.9	35.8	35.0
Pural_LDH 0.05wt% pH7	>1000	>1000	>1000	33.6	33.7	33.6
Pural_LDH 0.005wt% pH7	>1000	>1000	>1000	--	--	--
FG_LDH 5min	159.1	160.0	159.3	24.7	25.0	23.3

FG_LDH 10min	74.95	74.66	74.53	25.2	24.4	24.8
FG_LDH 15min	53.11	53.28	52.87	27.4	26.1	27.1
FG_LDH 20min	49.36	49.64	49.63	26.7	26.7	25.9
Pural0.05wt%pH7 after 1 EPD	>1000	>1000	>1000	22.6	19.6	21.4
Pural0.05wt%pH7 after 2 EPD	>1000	>1000	>1000	-4.42	-0.99	-5.01
FG_EPD 12.6. pH8 0 runs	73.85	74.82	77.04	16.7	17.2	15.7
FG_EPD 12.6. pH8 1 run	307.1	251.4	278.8	28.6	28.8	29.6
FG_EPD 12.6. pH8 2 runs	>1000	>1000	>1000	33.1	32.9	33.4
FG_EPD 12.6. pH8 3 runs	>1000	>1000	>1000	33.5	33.1	34.1
FG_EPD 12.6. pH8 4 runs	>1000	>1000	>1000	31.3	31.7	31.1
FG_LDH monowave 5min	194.3	196.6	193.8	28.2	27.9	27.2
FG_LDH monowave 10min	58.46	58.72	58.40	30.1	29.5	27.7
FG_LDH monowave 15min	55.03	53.90	54.24	26.7	27.7	28.0
FG_LDH monowave 20min	60.20	59.53	57.52	28.8	30.1	29.1
FG_LDH monowave 25min	58.13	58.30	59.10	29.8	28.2	29.4
FG_EPD 19.6. 0 cycles	55.91	56.23	55.93	27.1	25.2	24.7
FG_EPD 19.6. 1 cycle	295.4	306.3	321.0	34.9	31.0	33.5
FG_EPD 19.6. 0 cycles	902.8	>1000	879.4	33.9	35.4	35.8
FG_LDH EtOH	130.1	169.0	140.1	-4.21	-5.45	-5.57
FG_EPD LDH+PSS 0 cycles	132.6	131.4	132.9	-28.2	-27.7	-28.2
FG_EPD LDH+PSS 1 cycle	175.8	174.4	176.2	-18.6	-17.7	-16.1
FG_EPD LDH+PSS 2 cycles	195.0	196.9	193.4	-14.9	-15.0	-15.4
FG_EPD LDH+PSS 3 cycles	216.7	212.2	212.4	-14.6	-14.6	-14.6
FG_EPD 3.7. short run 0	63.86	64.83	64.23	30.9	29.7	29.8
FG_EPD 3.7. short run 1	105.2	105.4	--	29.6	29.8	30.9
FG_EPD 3.7. short run 2	190.9	207.9	190.4	30.7	31.9	32.7
FG_EPD 3.7. short run 3	344.8	349.9	308.9	30.1	31.0	31.6
FG_EPD 3.7. short run 4	724.7	841.1	811.7	25.5	24.7	24.2
FG_EPD 3.7. long run 0	64.58	64.75	63.44	30.2	28.8	28.6
FG_EPD 3.7. long run 1	219.5	238.9	224.3	30.3	31.9	32.1
FG_EPD 3.7. long run 2	547.6	920.0	861.0	21.3	22.5	23.9
FG_LDH 15.7.	110.0	109.2	112.6	--	--	--
FG_LDH PSS:CO3=1:1	--	--	--	15.2	12.6	14.2
FG_LDH onepot 30min	72.31	74.83	74.63	--	--	--
FG_LDH onepot 60min	75.38	78.29	78.72	--	--	--
FG_LDH onepot 90min	77.76	80.54	81.92	--	--	--
FG_LDH onepot 120min	80.64	82.15	83.54	--	--	--
FG_LDH monowave 30min	120.2	121.3	122.6	--	--	--
FG_LDH monowave 60min	121.6	123.5	122.1	--	--	--
FG_LDH monowave 90min	120.3	121.8	124.3	--	--	--
FG_LDH monowave 120min	119.2	120.9	121.8	--	--	--
FG_LDH onepot 17h	113.8	114.8	115.5	27.3	27.8	28.0
FG_LDH/PSS onepot 24h	687.4	>1000	>1000	14.9	14.8	14.4
FG_LDH onepot 24h	135.5	139.0	140.9	38.6	38.2	37.8
FG_LDH before PEG	23.4	23.4	23.8	--	--	--
FG_LDH after 2h PEG	31.3	30.3	29.4	--	--	--
FG_LDH onepot 24h 16.9.	119.0	113.8	113.6	38.9	39.2	40.2
FG_LDH+PEG monowave 3h	65.45	62.99	61.92	43.0	40.6	42.1

FG_LDH+PEG 19.9.	88.34	89.16	87.66	38.4	37.9	37.0
FG_LDH upscale 23.9.	112.6	112.1	110.9	39.0	41.8	40.2
Nanopore water	--	--	--	-0.48	-2.18	-2.15
DI water	--	--	--	-5.01	-11.5	-13.6
FG_LDH Line pH8	--	--	--	12.9	12.6	13.0
FG_LDH Line pH7	--	--	--	38.8	38.8	38.5
FG_LDH Line pH7 after EPD	114.7	112.0	112.2	38.9	39.1	40.7

6.1.12. Gas pycnometry

Table 12: measurements obtained by gas pycnometry

Cycle	**Volume [cm³]**	**Density [g/cm³]**
1	1.8599	1.5670
2	1.8624	1.5649
3	1.8602	1.5667
4	1.8620	1.5652
5	1.8612	1.5659
6	1.8637	1.5638
7	1.8619	1.5654
8	1.8653	1.5625
9	1.8647	1.5630
10	1.8641	1.5635

6.2. Table of figures

Figure 1: From left to right: nacreous layer on the inside of a Nautilus shell; micrograph of aragonite platelets within the nacre structure; aragonite nanocrystals (white) & interlamellar space with organic mortar (grey). 8
Figure 2: Models for interfacial sliding resistance, from left to right: mineral bridge model; surface roughness model; platelet interlocking model. Arrows represent platelet movement relative to one another. 9
Figure 3: Left: An idealized FRP material under no mechanical stress: fibres are black, matrix is light blue. Middle: tensile stress causes breakage of individual fibres, load transfer to neighbouring fibres depicted in orange, no macroscopic damage. Right: formation of a critical cluster causes cascading and therefore catastrophic failure of the material, visualized in red. 9
Figure 4: A graphical representation of the process used by de Luca. 10
Figure 5: The LDH structure alongside its intercalants. 11
Figure 6: left: anodic EPD; right: cathodic EPD 12
Figure 7: left: after surface detection, the concave sedimentation probe is immersed within the examined suspension. Middle: upon complete immersion of the measurement probe, mass data acquisition will commence. Right: over time, any given unstable suspension will result in an increase of recorded mass over time. 16
Figure 8: Diagram (left) and picture (right) of the laboratory scale setup used for aqueous deposition. 17
Figure 9: Top: Diagram of the EPD cell used for experiments involving the K03 composite line. Bottom: side view of the EPD cell used for experiments involving the K03 composite line. 17
Figure 10: Schematic of the k03 composite line used for scaled manufacturing, alongside photos of individual line components, from left to right: EPD bath, PEI infiltration bath, IR furnaces, heated shear pins. 18
Figure 11: Graphical representation of the factor between projected and real particle, dependant upon distance from fibre centre. 19
Figure 12: SEM micrographs of synthesized LDH particles (24 h reflux treatment) deposited on aluminium foil. 21

Figure 13: left: histogram of particle size in SEM micrographs depicted in Figure 12. Right: Particle size of samples with 2h reflux time (black) and 24h reflux time (red), measured by DLS..... 21
Figure 14: left: measured and calculated powder diffraction pattern of LDH. Right: unit cell of LDH. Bonds and intercalated carbonate anions were omitted for visual reasons. Hydrogen atoms are depicted in white, oxygen atoms in red, metals in silver/orange. Unit cell and calculated pattern were obtained from Crystallography open database (COD ID: 9009272). 22
Figure 15: black: LDH as synthesized, red: commercially obtained LDH (Pural), blue: synthesized LDH recovered from working electrode after EPD..... 23
Figure 16: TGA data for synthesized (green) and commercially obtained LDH (red). 24
Figure 17: LDH usage per EPD cycle. One cycle equates to 20 cm of coated carbon fibres. 26
Figure 18: left: particles deposited on a carbon fibre using the scaled setup. Right: particle size distribution of particles located up to 1.3 and -1.6 µm away from the centre of the fibre. Accordingly, particle size was adjusted by factor 1.033. 27
Figure 19: SEM micrographs of samples produced at bench scale (5 min, 5 V, 0 A), displaying an even monolayer LDH coating on carbon fibres..... 27
Figure 20: SEM micrographs of samples produced at the k03 composite line (line speed: 0.6 m/min, 30 V, 0.03 A). The coating quality is influenced by manufacturing conditions, coated fibres are being subjected to abrasive conditions during bends under tension. 28
Figure 21: Macroscopic electrophoretic deposition of LDH from 72 vol% ethanolic suspension. 28
Figure 22: Electrocoagulation can form thicker LDH coatings in aqueous environments than EPD. 30
Figure 23: Sand rose formations of different platelet size grown on carbon fibres. Left: 5 V, 0.18 A, 30 min. Right: 5 V, 0.18 A, 5 min..... 30
Figure 24: left: sand rose layer, incompletely covered by horizontally stacked LDH. Right: fully developed layer of horizontally stacked, in situ grown LDH. Both coatings were grown at 5 V, 0.18 A, 30 min..... 30

Figure 25: SEM micrograph displaying bare carbon fibre surface (top), sand rose layer (middle) and horizontally stacked top layer of LDH. Cross section is likely the result of a neighbouring fibre's imprint. Experimental conditions: 5 V, 0.18 A, 5 min. 31
Figure 26: first (left) and second (right) production run of CF/LDH/PEI composite tapes at the k03 composite line. Green dots represent tape sections which meet the width requirement for consolidation. The blue section represents the FVF requirement for consolidation. 31
Figure 27: Fibre alignment angle distribution of CF/LDH/PEI composite laminate. .. 32
Figure 28: Optical micrographs of CF/LDH/PEI composite laminate sectioned at an angle of 5°. 32
Figure 29: left: CF/LDH/PEI laminate test specimens after ILSS testing. Right: load over extension for all tested CF/LDH/PEI specimens. 33
Figure 30: from left to right and top to bottom: FTIR spectra of Pural LDH, LDH peptized above ambient pressure, LDO from thermal oxidation of LDH, LDH peptized at ambient pressure, LDH after lyophilisation and after EPD 36
Figure 31: from left to right and top to bottom: FTIR spectra of LDH peptized at ambient pressure, pristine CF, CF after EPD 37
Figure 32: ILSS testing results of each individual specimen tested. 38
Figure 33: sedimentation as mass over time for water (graph 1 to 4) and LDH:PSS=1:9 suspensions (graph 5 and 6) 39
Figure 34: sedimentation as mass over time for synthesized LDH (ambient pressure) at pH 7 (graph 1 to 3) and pH 8 (graph 4 to 6) 40
Figure 35: sedimentation as mass over time for synthesized LDH (ambient pressure) at pH 9 (graph 1 to 3) and for synthesized LDH (ambient pressure) at pH 7 before the suspension was used for EPD (graph 4 to 6) 41
Figure 36: sedimentation as mass over time for synthesized LDH (ambient pressure) at pH 7 after the suspension was used for EPD. Random measurement error larger than other measurements because of outside influences during measurement. 42
Figure 37: TGA data for synthesized and commercially obtained LDH (graph 1 and 2), for carbon fibres after LDH deposition through EPD (graph 3 to 5) and for pristine carbon fibres (graph 6). Noise in graph 3 and 4 likely from LDH decomposition and delamination from CF surface. 43

6.3. Bibliography

1. Hasan, M., Zhao, J. & Jiang, Z. Micromanufacturing of composite materials: a review. *Int. J. Extreme Manuf.* **1**, 012004 (2019).
2. Hardy, R. *Longbow: A Social and Military History*. (Bois d'Arc Press, 1992).
3. Pickering, K. *Properties and Performance of Natural-Fibre Composites*. (Elsevier, 2008).
4. Bledzki, A. K., Sperber, V. E. & Faruk, O. *Natural and Wood Fibre Reinforcement in Polymers*. vol. 13 (iSmithers Rapra Publishing, 2002).
5. McMullen, P. Fibre/resin composites for aircraft primary structures: a short history, 1936–1984. *Composites* **15**, 222–230 (1984).
6. Shindo, A. Studies on graphite fibre. *Jpn. Gov't Ind Res Inst Osaka Jpn. Rpt No 317* 1–50 (1961).
7. Reux, F. Worldwide composites market: Main trends of the composites industry. *5th Innov. Compos. Summit-JEC ASIA 2012* 26–28 (2012).
8. Joshi, S. V., Drzal, L. T., Mohanty, A. K. & Arora, S. Are natural fiber composites environmentally superior to glass fiber reinforced composites? *Compos. Part Appl. Sci. Manuf.* **35**, 371–376 (2004).
9. Steger, J. Light weight! No matter what the costs? Plant fibres for light weight automotive applications. *J. Biobased Mater. Bioenergy* **4**, 181–184 (2010).
10. Yang, Y. *et al.* Recycling of composite materials. *Chem. Eng. Process. Process Intensif.* **51**, 53–68 (2012).
11. Netravali, A. N. & Chabba, S. Composites get greener. *Mater. Today* **6**, 22–29 (2003).
12. Qian, H., Greenhalgh, E. S., Shaffer, M. S. & Bismarck, A. Carbon nanotube-based hierarchical composites: a review. *J. Mater. Chem.* **20**, 4751–4762 (2010).

13. Gorbatikh, L., Wardle, B. L. & Lomov, S. V. Hierarchical lightweight composite materials for structural applications. *Mrs Bull.* **41**, 672–677 (2016).
14. Karger-Kocsis, J., Mahmood, H. & Pegoretti, A. All-carbon multi-scale and hierarchical fibers and related structural composites: A review. *Compos. Sci. Technol.* **186**, 107932 (2020).
15. Fratzl, P. & Weinkamer, R. Nature's hierarchical materials. *Prog. Mater. Sci.* **52**, 1263–1334 (2007).
16. Sun, J. & Tong, J. Fracture Toughness Properties of Three Different Biomaterials Measured by Nanoindentation. *J. Bionic Eng.* **4**, 11–17 (2007).
17. Sun, J. & Bhushan, B. Hierarchical structure and mechanical properties of nacre: a review. *RSC Adv* **2**, 7617–7632 (2012).
18. Aksay, I. A. *et al.* Biomimetic Pathways for Assembling Inorganic Thin Films. *Science* **273**, 892–898 (1996).
19. Kakisawa, H. & Sumitomo, T. The toughening mechanism of nacre and structural materials inspired by nacre. *Sci. Technol. Adv. Mater.* **12**, 064710 (2012).
20. Li, X. & Huang, Z. Unveiling the Formation Mechanism of Pseudo-Single-Crystal Aragonite Platelets in Nacre. *Phys. Rev. Lett.* **102**, 075502 (2009).
21. Oaki, Y., Kotachi, A., Miura, T. & Imai, H. Bridged Nanocrystals in Biominerals and Their Biomimetics: Classical Yet Modern Crystal Growth on the Nanoscale. *Adv. Funct. Mater.* **16**, 1633–1639 (2006).
22. Jackson, A. P., Vincent, J. F. V., Turner, R. M. & Alexander, R. M. The mechanical design of nacre. *Proc. R. Soc. Lond. B Biol. Sci.* **234**, 415–440 (1997).
23. Currey, J. D. Mechanical Properties of Mother of Pearl in Tension. *Proc. R. Soc. Lond. Ser. B* **196**, 443–463 (1977).

24. Evans, A. G. *et al.* Model for the robust mechanical behavior of nacre. *J. Mater. Res.* **16**, 2475–2484 (2001).
25. Meyers, M. A., Lin, A. Y.-M., Chen, P.-Y. & Muyco, J. Mechanical strength of abalone nacre: role of the soft organic layer. *J. Mech. Behav. Biomed. Mater.* **1**, 76–85 (2008).
26. Barthelat, F., Li, C.-M., Comi, C. & Espinosa, H. D. Mechanical properties of nacre constituents and their impact on mechanical performance. *J. Mater. Res.* **21**, 1977–1986 (2006).
27. Katti, K. S., Katti, D. R., Pradhan, S. M. & Bhosle, A. Platelet interlocks are the key to toughness and strength in nacre. *J. Mater. Res.* **20**, 1097–1100 (2005).
28. Tang, Z., Kotov, N. A., Magonov, S. & Ozturk, B. Nanostructured artificial nacre. *Nat. Mater.* **2**, 413–418 (2003).
29. Barthelat, F. & Zhu, D. A novel biomimetic material duplicating the structure and mechanics of natural nacre. *J. Mater. Res.* **26**, 1203–1215 (2011).
30. Sharma, M. *et al.* Carbon fiber surfaces and composite interphases. *Compos. Sci. Technol.* **102**, 35–50 (2014).
31. Fuwa, M., Bunsell, A. R. & Harris, B. Tensile failure mechanisms in carbon fibre reinforced plastics. *J. Mater. Sci.* **10**, 2062–2070 (1975).
32. Tang, L.-G. & Kardos, J. L. A review of methods for improving the interfacial adhesion between carbon fiber and polymer matrix. *Polym. Compos.* **18**, 100–113 (1997).
33. De Luca, F. *et al.* Nacre-nanomimetics: strong, stiff, and plastic. *ACS Appl. Mater. Interfaces* **7**, 26783–26791 (2015).

34. De Luca, F., Sernicola, G., Shaffer, M. S. & Bismarck, A. “Brick-and-Mortar” nanostructured interphase for glass-fiber-reinforced polymer composites. *ACS Appl. Mater. Interfaces* **10**, 7352–7361 (2018).
35. De Luca, F. *et al.* Increasing carbon fiber composite strength with a nanostructured “brick-and-mortar” interphase. *Mater. Horiz.* **5**, 668–674 (2018).
36. Evans, D. G. & Slade, R. C. T. Structural Aspects of Layered Double Hydroxides. in *Layered Double Hydroxides* (eds. Duan, X. & Evans, D. G.) 1–87 (Springer Berlin Heidelberg, Berlin, Heidelberg, 2006). doi:10.1007/430_005.
37. Besra, L. & Liu, M. A review on fundamentals and applications of electrophoretic deposition (EPD). *Prog. Mater. Sci.* **52**, 1–61 (2007).
38. Avgustinik, A., Vigdergauz, V. & Zhuravlev, G. Electrophoretic deposition of ceramic masses from suspensions and calculation of deposit yields. *J Appl Chem USSR Engl. Transl.* **35**, 2175–80 (1962).
39. Xu, Z. P., Stevenson, G., Lu, C.-Q. & Lu, G. Q. (Max). Dispersion and Size Control of Layered Double Hydroxide Nanoparticles in Aqueous Solutions. *J. Phys. Chem. B* **110**, 16923–16929 (2006).
40. Ma, R. & Sasaki, T. Nanosheets of Oxides and Hydroxides: Ultimate 2D Charge-Bearing Functional Crystallites. *Adv. Mater.* **22**, 5082–5104 (2010).
41. Wang, Q. & O’Hare, D. Recent Advances in the Synthesis and Application of Layered Double Hydroxide (LDH) Nanosheets. *Chem. Rev.* **112**, 4124–4155 (2012).
42. Molano-Mendoza, M. *et al.* Synthesis of Mg-Al layered double hydroxides by electrocoagulation. *MethodsX* **5**, 915–923 (2018).
43. Yurgartis, S. W. Measurement of small angle fiber misalignments in continuous fiber composites. *Compos. Sci. Technol.* **30**, 279–293 (1987).

44. Bernard, E., Zucha, W. J., Lothenbach, B. & Mäder, U. Stability of hydrotalcite (Mg-Al layered double hydroxide) in presence of different anions. *Cem. Concr. Res.* **152**, 106674 (2022).
45. Aramendía, M. A. *et al.* Comparative study of Mg/Al and Mg/Ga layered double hydroxides. *Microporous Mesoporous Mater.* **29**, 319–328 (1999).
46. Forano, C., Costantino, U., Prévot, V. & Gueho, C. T. Chapter 14.1 - Layered Double Hydroxides (LDH). in *Developments in Clay Science* (eds. Bergaya, F. & Lagaly, G.) vol. 5 745–782 (Elsevier, 2013).
47. P.K. Mallick. *Fibre-Reinforced Composites: Materials, Manufacturing and Design.* (CRC Press; Boca Raton, FL, USA, 2007).
48. Jin, L. *et al.* Insights into memory effect mechanisms of layered double hydroxides with solid-state NMR spectroscopy. *Nat. Commun.* **13**, 6093 (2022).
49. Moujahid, E. M., Leroux, F., Dubois, M. & Besse, J.-P. In situ polymerisation of monomers in layered double hydroxides. *Comptes Rendus Chim.* **6**, 259–264 (2003).